Modeling of Dense Water Production and Salt Transport from Alaskan Coastal Polynyas

Sergio R. Signorini
SAIC General Sciences Corporation
Beltsville, Maryland

Donald J. Cavalieri
Laboratory for Hydrospheric Processes
NASA Goddard Space Flight Center
Greenbelt, Maryland

The main significance of this paper is that a realistic, three-dimensional, high-resolution primitive equation model has been developed to study the effects of dense water formation in Arctic coastal polynyas. The model includes realistic ambient stratification, realistic bottom topography, and is forced by time-variant surface heat flux, surface salt flux, and time-dependent coastal flow. The salt and heat fluxes, and the surface ice drift, are derived from satellite observations (SSM/I and NSCAT sensors). The model is used to study the stratification, salt transport, and circulation in the vicinity of Barrow Canyon during the 1996/97 winter season. The coastal flow (Alaska coastal current), which is an extension of the Bering Sea throughflow, is formulated in the model using the wind-transport regression. The results show that for the 1996/97 winter the northeastward coastal current exports 13% to 26% of the salt produced by coastal polynyas upstream of Barrow Canyon in 20 to 30 days. The salt export occurs more rapidly during less persistent polynyas. The inclusion of ice-water stress in the model makes the coastal current slightly weaker and much wider due to the combined effects of surface drag and offshore Ekman transport.

Submitted to the *Journal of Geophysical Research*, 2000.

Modeling of Dense Water Production and Salt Transport from Alaskan Coastal Polynyas

Sergio R. Signorini
SAIC General Sciences Corporation, Beltsville, Maryland.

Donald J. Cavalieri
Laboratory for Hydrospheric Processes, NASA Goddard Space Flight Center, Greenbelt, Maryland

Abstract

A three-dimensional, primitive equation model was used to assess the effects of dense water formation from winter (1996/1997) polynyas on the stratification, salt transport, and circulation in the vicinity of Barrow Canyon. The model includes ambient stratification, bottom topography, and is forced by time-variant surface heat flux, surface salt flux, and time-dependent coastal flow. The influence of sea ice on the circulation and salt transport is also analyzed by prescribing ice-water stress at the sea surface. The salt and heat fluxes, and the surface ice drift, are derived from satellite observations (SSM/I and NSCAT sensors). The coastal flow (Alaska coastal current), which is an extension of the Bering Sea throughflow, is formulated in the model using the wind-transport regression. Two types of numerical experiments were conducted. One set of experiments was forced by strong and persistent polynyas, simulated by 20-day averaged heat and salt fluxes originating from the largest events, and another set of experiments was forced by weaker and less persistent polynyas using time-dependent forcing. The results show that the northeastward coastal current can export 13 to 26% of the salt produced by polynyas upstream of Barrow Canyon in 20 to 30 days. The salt export occurs more rapidly during less persistent polynyas. The inclusion of ice-water stress in the model makes the coastal current slightly weaker and much wider due to the combined effects of surface drag and offshore Ekman transport. However, the effect of sea ice drift on the salt advection is relatively small. During the more persistent polynya event (December 17, 1996 to January 7, 1997), 380×10^9 kg of salt were produced in 20 days and 112×10^9 kg (30%) of salt were exported offshore of the generation area. Salt advection by the coastal current was 17%, while the other 13% were due to a combination of gravitational circulation and lateral diffusion. During the less persistent polynya event (January 28-February 28, 1997), 223×10^9 kg of salt were produced in 32 days and 127×10^9 kg were exported offshore. For this rapidly changing event, 26% of the total salt generated was exported via advection by the coastal current and about 31% was exported via a combination of gravitational flow, Ekman transport, and lateral diffusion. A shallow halocline ($\sim$30 m), formed during the previous summer-fall melt, limits convective mixing within the upper 30 meters, except for near the coast and the shallow shelf where horizontal current shear and bottom layer turbulence erodes the shallow halocline. The salinity of the dense water ($\sim$31 psu) simulated by

the model for the 1996/1997 winter was not large enough to ventilate the Arctic halocline, which has a salinity of 34 psu at a depth of approximately 200 meters. However, the ambient surface salinity in the vicinity of Point Barrow may occasionally reach 32 psu, which, combined with vigorous ice growth (about 4 meters), can generate dense water with salinities of about 34 psu and ventilate the Arctic halocline. We suggest future studies, using the upgraded version of the model developed in this investigation, to address these extreme episodical events that occur during certain winters with an extended regional domain to include polynya generation areas farther to the east (e.g., Mackenzie Bay).

1. Introduction

The purpose of this study is to estimate the effects of Arctic coastal polynyas on the circulation and stratification of the western Arctic Ocean. These polynyas, which are located over the continental shelves of the peripheral seas of the Arctic Ocean, provide a mechanism for the growth of large amounts of ice in limited geographic areas and thus contribute relative large amounts of brine to the halocline layer. Recurrent polynyas form on the Canadian and Alaskan coasts from Banks Island to the Bering Strait and on the Siberian coast from the Bering Strait to the New Siberian Islands. Two regions that account for almost 50% of the total dense water production are the Siberian coastal polynyas in the adjacent regions of the Gulf of Anadyr and Anadyr Strait and the Alaskan coastal polynyas which occur along the coast from Cape Lisburne to Point Barrow. All the combined western Arctic coastal polynyas account for a mean annual brine flux of 0.5 ± 0.2 Sv. Combination of this flux with the contribution from the Barents, Kara, and Laptev Seas, shows that over the entire Arctic coastal polynyas generate about 0.7-1.2 *Sv* of dense water [*Cavalieri and Martin*, 1994].

Another objective of this study is to analyze the effects of bottom topography in the channeling of dense water from the coastal polynyas on the shelves to the Arctic halocline. For example, during February 1992 an intense storm generated a large region of low ice concentration in the eastern Chukchi Sea over Barrow Canyon. The refreezing of the region was followed by a flow of a dense plume down Barrow Canyon [*Cavalieri and Martin*, 1994]. This study addresses the ocean dynamical response to these events and evaluates their impact on the Arctic Ocean halocline.

It is well known that there are large lateral influxes of shelf waters to the central basins of the Arctic Ocean. These influxes originate from the formation of dense water on the shelves during winter through brine rejection associated with freezing of sea water in coastal polynyas. The Canadian Basin has as its source low-salinity Pacific waters that have entered the Arctic Ocean through the Bering Strait, cooled, and then had their salinity increased on the shelf [*Aagaard and Carmac*, 1994]. *Weingartner et al.*, [1998] showed that most of the dense water formed on the Chukchi shelf in 1991-1992 flowed into the Arctic Ocean through Barrow Canyon. The fate of the plume of dense water depends on the volume of ambient shelf and slope water that the plume entrains as it sinks. The saltier, swifter along canyon flow hugged the eastern wall of the canyon and the isohalines tilted upward to the east. Their results suggest a gravity current wherein rotation and bottom friction are important dynamically, but entrainment is not.

Previous modeling studies [*Chapman and Gawarkiewicz*, 1995; *Gawarkiewicz and Chapman*, 1995] addressed the problem of dense water formation and transport on shallow sloping shelves and canyons. These studies focussed on process-oriented experiments with idealized topography and non-stratified far fields. Some modeling studies of outflow of dense water have considered spatially structured (stratified) water bodies but stagnant ambient flow [*Junkclaus and Backhaus*, 1994; Junkclaus et al., 1995]. In the present study we conduct our numerical experiments using realistic topography, ambient stratification, and ambient flow for the Chukchi and Beaufort Seas using a high resolution numerical grid (1 to 5 km). The focus of our analysis is Barrow Canyon where most of the dense water formed on the Chukchi shelf is channeled into the Arctic Ocean [*Weingartner et al.*, 1999].

2. Data Sources

2.1. Meteorological and Oceanic Data

The meteorological data required for this study, consisting of wind speed and direction, specific humidity, surface pressure, and air temperature, were obtained from the NOAA's National Center for Environmental Prediction (NCEP). These daily data originate from the NCEP/NCAR 40-year reanalysis project (*Kalnay et al.*, 1994) and were used to calculate the daily surface heat flux. The daily wind speed and direction were also used to derive the Bering Strait throughflow transport using the formulation given by *Coachman and Aagaard* [1988]. The hydrographic data of *Carmack and Münchow* [1997] were used to initialize the salinity and temperature fields for the model.

2.2. Satellite Data

The model does not include an explicit formulation for sea ice. Instead, satellite-derived sea ice concentrations provide a measure of the open water within leads and polynyas needed to calculate F_T and F_S. The sea ice concentrations are computed from daily gridded radiances obtained from the special sensor microwave/imager (SSM/I) onboard the DMSP F13 satellite using a modified version of the NASA Team

sea ice algorithm designed to lessen the low ice concentration bias resulting from the presence of new and young sea ice (Cavalieri, 1994). This so-called thin ice algorithm has been used previously in a study of dense water production in the Okhotsk Sea polynyas (Martin et al., 1998). Using the SSM/I sea ice concentrations (C), the measured open water amount (1-C) is computed each day for the 1996/97 winter for all 25-km grid cells within the study region (Figure 1). A time series of daily open water amounts for the entire study region is presented in Figure 2 for the period of December 1, 1996 through April 29, 1997. Five major polynya events can be identified in this time series with open water areas greater than 3000 km^2: two in December 1996, and one each in January, February, and April, 1997, respectively.

Arctic sea ice displacements for the 1996/97 winter period were obtained from the processing of satellite data sets. The methods employed to derive the ice displacements from merged DMSP SSM/I and ADEOS NSCAT data sets are fully described by Liu et al. (1999). The ice displacements were computed by applying wavelet analysis to SSM/I and NSCAT 85-GHz and 13.9-GHz radiance maps, respectively. Both sensors provide compatible daily sea ice drift maps, but NSCAT provides somewhat better results when cloud or surface effects are present in the SSM/I data. NSCAT responds to changes in surface roughness, while the SSM/I measures differences in brightness temperature. Liu et al. also provide an estimate of the accuracy of the satellite-derived sea ice drift from a comparison with Arctic Ocean buoy data. The comparison between NSCAT derived ice drift and that from buoy data yields a 2.8 cm s^{-1} rms difference of speeds and a 28.6° rms difference of drift direction. A comparison of SSM/I derived drifts with buoy data yields a 3.0 cm s^{-1} rms difference of speeds and a 34.4° rms difference of drift direction. The latter results are similar to those obtained in an earlier study with SSM/I data (Liu and Cavalieri, 1998).

A time sequence of daily surface salt fluxes for February 12-19, 1997, is shown in Figure 3. The ice drift vectors are superimposed on salt flux maps. The salt fluxes shown in this figure were computed using the formulation described in section 2.3 and using ice concentrations from the original NASA Team algorithm (Cavalieri et al., 1984; Gloersen and Cavalieri, 1986) which is particularly sensitive to the presence of new and young ice types. While the original algorithm overestimates open water amount (and thus not used in computing the surface fluxes) in polynyas because of the presence of thin ice types, it provides a useful visualization of the spatial and temporal variability of the Alaskan coastal polynyas for the 1996/97 winter. For example, Figure 3 clearly shows the opening and closing of the polynya during the February event, with major brine rejection occurring on February 17, 1997. The surface extent of the polynya brine rejection area for the two strongest polynya events (December 17, 1996 - January 6, 1997) is shown in Figure 4. The averaged salt flux distribution, averaged over the 20 days during which these two strongest polynyas occurred, is shown within the model grid domain. The white line delimits the control volume to be used for the total salt variability analysis based on the model predictions. The three thick black lines show the location of the Barrow Canyon transects extracted from the model output to be analyzed in terms of stratification and velocity changes caused by the polynyas.

2.3. Calculation of Heat and Salt Fluxes

The surface heat (F_T) and salt (F_S) fluxes are calculated following the method of *Cavalieri and Martin* [1994]. The daily total heat loss H_L in Joules is obtained by

$$H_L = (8.64 \times 10^4) A F_{net} \tag{1}$$

where A is the open water area as measured by SSM/I for a given grid cell and day and F_{net} is the total ocean-to-atmosphere heat flux [*Cavalieri and Martin*, 1994] in J m^{-2} s^{-1}. The volume of ice production in cubic meters per grid cell per day is given by

$$V_I = H_L / \rho_i L \tag{2}$$

where ρ_i is the density of ice (920 kg m^{-3}) and L is the latent heat of fusion (3.34×10^5 J kg^{-1}).

The salt production in kilograms per grid cell per day is given by

$$S_F = \rho_i V_I (S_w - S_i) 10^{-3} \tag{3}$$

where S_w is the salinity of sea water and S_i is the salinity of frazil ice, both in psu. The salinity of frazil ice is calculated from $S_i = 0.31 S_w$ [*Martin and Kaufman*, 1981].

The units of F_T and F_S are originally Kg d^{-1} and J d^{-1}, respectively. These units were converted to m s^{-1} psu and m s^{-1} °C, respectively, to conform with the units required by (1) and (2). The conversion was done using

$$F_T = H_L/(8.64 \times 10^4 A \rho_w c_p) \quad (4)$$

$$F_S = 10^3 S_F/(8.64 \times 10^4 A \rho_i) \quad (5)$$

where c_p is the specific heat of sea water (4186 J kg^{-1} $^oC^{-1}$) and ρ_w is the density of sea water in kg m^{-3}. Sea water density ρ_w is calculated from salinity, temperature, and pressure using the equation of state formulation derived by Jackett and McDougall (1992, unpublished manuscript) adopted for the ocean model.

3. Model Approach

We use a three-dimensional, rigid lid, primitive equation model with orthogonal curvilinear coordinates in the horizontal and a generalized coordinate in the vertical (S Coordinate Primitive Equation Model, SPEM5.1). The generalized vertical coordinate allows high resolution in the upper ocean while maintaining the bathymetry-following properties of the σ coordinate [*Song and Haidvogel*, 1994]. Table 1 shows the level thicknesses at minimum depth, at the slope, and at the maximum depth to illustrate the stretching of vertical resolution across the grid domain. The model was previously applied and validated in the Barrow Canyon region [*Signorini et al.*, 1997].

3.1. Governing Equations

The primitive equations in Cartesian coordinates governing the model dynamics are

$$\frac{\partial u}{\partial t} + \vec{V} \cdot \nabla u - fv =$$

$$-\frac{\partial \phi}{\partial x} + \frac{\partial}{\partial x}\left[K_h \frac{\partial u}{\partial x}\right] + \frac{\partial}{\partial y}\left[K_h \frac{\partial u}{\partial y}\right] + \frac{\partial}{\partial z}\left[K_v \frac{\partial u}{\partial z}\right] \quad (6)$$

$$\frac{\partial v}{\partial t} + \vec{V} \cdot \nabla v + fu =$$

$$-\frac{\partial \phi}{\partial y} + \frac{\partial}{\partial x}\left[K_h \frac{\partial v}{\partial x}\right] + \frac{\partial}{\partial y}\left[K_h \frac{\partial v}{\partial y}\right] + \frac{\partial}{\partial z}\left[K_v \frac{\partial v}{\partial z}\right] \quad (7)$$

$$\frac{\partial T}{\partial t} + \vec{V} \cdot \nabla T =$$

$$\frac{\partial}{\partial x}\left[K_h \frac{\partial T}{\partial x}\right] + \frac{\partial}{\partial y}\left[K_h \frac{\partial T}{\partial y}\right] + \frac{\partial}{\partial z}\left[K_{TS} \frac{\partial T}{\partial z}\right] \quad (8)$$

$$\frac{\partial S}{\partial t} + \vec{V} \cdot \nabla S =$$

$$\frac{\partial}{\partial x}\left[K_h \frac{\partial S}{\partial x}\right] + \frac{\partial}{\partial y}\left[K_h \frac{\partial S}{\partial y}\right] + \frac{\partial}{\partial z}\left[K_{TS} \frac{\partial S}{\partial z}\right] \quad (9)$$

$$\rho = \rho(T, S, P) \quad (10)$$

$$\frac{\partial \phi}{\partial z} = -\frac{\rho g}{\rho_o} \quad (11)$$

$$\frac{\partial u}{\partial x} + \frac{\partial v}{\partial y} + \frac{\partial w}{\partial z} = 0 \quad (12)$$

where

(u, v, w) = the (x, y, z) components of vector velocity $\vec{V}$

$\rho_o + \rho(x, y, z, t)$ = total *in situ* density

$T(x, y, z, t)$ = potential temperature

$S(x, y, z, t)$ = salinity

P = total pressure $P \approx -\rho g z$

$\phi(x, y, z, t)$ = dynamic pressure $\phi = (P/\rho)$

$f(x, y)$ = Coriolis parameter

g = acceleration of gravity

(K_h, K_v, K_{TS}) = horizontal and vertical eddy diffusion coefficients

3.2. Surface Forcing

The grid has been adapted and expanded for the polynya investigation to include the brine formation areas of the Chukchi Sea (Figure 1). The initial and open boundary conditions are essentially the same as in [*Signorini et al.*, 1997]. The boundary conditions for surface heat and salt fluxes were formulated as

$$K_{TS} \frac{\partial T}{\partial z} = F_T \quad (13)$$

$$K_{TS} \frac{\partial S}{\partial z} = F_S \quad (14)$$

where K_{TS} is in m^2/s , T is in ^oC, S is in psu, and F_T and F_S are the surface heat and salt fluxes, respectively. The vertical eddy diffusivity K_v is calculated following *Pacanowski and Philander*, [1981]

$$K_v = \frac{\nu_o}{(1 + \alpha R_i)^n} + \nu_b \quad (15)$$

$$K_{TS} = \frac{K_v}{(1+\alpha R_i)} + \kappa_b \tag{16}$$

where R_i is the Richardson number, ν_b and κ_b are background dissipation parameters and ν_o, α and n are adustable parameters. These were set to

$$\nu_o = 0.01 \text{ m}^2 \text{ s}^{-1},\ n = 2,\ \alpha = 5$$
$$\nu_b = 10^{-4} \text{ m}^2 \text{ s}^{-1},\ \kappa_b = 10^{-5} \text{ m}^2 \text{ s}^{-1}$$

The heat and salt fluxes at the top layer of the model are assumed zero when the grid cells are totally ice covered and the water temperature is set to its freezing value (T^{ice}) according to

$$T^{ice} = 0.094 - 0.00753p - 0.057S \tag{17}$$

where p is given in bars and S is the salinity in psu [*Millero*, 1975]. For grid cells containing open water F_T and F_S are imposed at the top layer following (13) and (14).

Surface ice-water stress was implemented in the model to evaluate the effect of ice drift on the circulation and salt transport. The ice water stress was calculated from satellite-derived ice drift data, as described in section 2.2, using the following formulation,

$$\tau^x_{iw} = C_{iw}\overline{U}_{iw}\left[u_i - u_w\right]C \tag{18}$$

$$\tau^y_{iw} = C_{iw}\overline{U}_{iw}\left[v_i - v_w\right]C \tag{19}$$

$$\overline{U}_{iw} = \left[\left(u_i - u_w\right)^2 + \left(v_i - v_w\right)^2\right]^{\frac{1}{2}} \tag{20}$$

where τ^x_{iw} and τ^y_{iw} are the ice-water stress components, $C_{iw} = 5.5 \times 10^{-3}$ is the ice-water drag coefficient, u_i and v_i are the ice drift velocity components, u_w and v_w are the surface water velocity components, and C is the ice concentration. The boundary conditions for ice-water stress momentum transfer are formulated as

$$K_\nu \frac{\partial u}{\partial z} = \frac{\tau^x_{iw}}{\rho} \tag{21}$$

$$K_\nu \frac{\partial v}{\partial z} = \frac{\tau^y_{iw}}{\rho} \tag{22}$$

3.3. Coastal Flow

The Alaskan coastal flow in the Chukchi Sea is primarily influenced by the flow through Bering Strait. The mean Bering Strait northward transport was estimated at 1 Sv [*Coachman et al.*, 1975], and this influx is a major consequence of the density structure of the Arctic Ocean [*Coachman and Barnes*, 1961; *Aagaard et al.*, 1981; *Killworth and Smith*, 1984]. The mean flow appears driven by the sea surface slope downward toward the north of the order of 10^{-6} [*Coachman and Aagaard*, 1966] which is probably of steric origin [*Coachman et al.*, 1975; *Stigebrandt*, 1984] and associated with the mean density difference between the North Pacific and the Arctic Ocean. However, there is substantial evidence of atmospherically forced major variability in the flow, including reversals to southward transport [*Aagaard et al.*, 1985].

Coachman and Aagaard [1988] suggest the following transport equation for the Bering Strait flow

$$Tr = 1.06 - 0.112W \tag{23}$$

where Tr is the transport in sverdrups and W is the component of the surface wind along 192°T in meters per second. We use daily NCEP winds near Bering Strait to calculate the time-varying transport. The Cape Lisburne transport is taken to be 1/3 of the Bering Strait transport and is used to force the model coastal flow in the vicinity of Cape Lisburne (T. Weingartner's personal communication). Figure 5 shows a time-series stack of the daily east and north wind components in Bering Strait, the wind component towards 192°T in Bering Strait, the derived Bering Strait volume transport, and the derived Cape Lisburne volume transport for January-March, 1997. Note that the wind component towards 192°T in Bering Strait and the volume transport in Bering Strait and Cape Lisburne are inversely correlated [*Aagaard et al.*, 1985]. The Cape Lisburne transport exhibits significant variability. The largest sustained transport occurs in January when the winds were weaker in Bering Strait. The January-March average transport is about 0.25 Sv. In our numerical experiments we use time-variant and steady coastal flow forcing. The steady coastal flow is obtained by averaging the time-variant transport at Cape Lisburne over the entire duration of the run prior to each

numerical simulation. Differences between the two methods are analyzed in section 4.

4. Model Experiments and Discussion

A series of seven numerical experiments were conducted to determine the effects of different combinations of model forcing on the salt transport, stratification, and circulation. These include runs with and without coastal flow and runs with and without heat and salt surface fluxes. The forcing was also configured for time-averaged and time-varying coastal flow and surface fluxes. The experiments can be divided into two major categories, those conducted with time-averaged surface flux forcing, and those conducted with time-variant flux forcing. Several forcing combinations were imposed under each of these two major categories. One experiment also included surface momentum forcing from ice-water stresses. The forcing fields were spatially interpolated off-line from 25 km resolution to the grid resolution of the model, which averages 3 km. The daily fluxes and ice drift were then linearly interpolated on-line to the time resolution required by the model time steps (2 minutes). Table 2 summarizes all experiment cases. Cases 1 through 4 fall in the first category and were designed to evaluate the impact of strong polynya events on the circulation, stratification, and salt generation in the study region. Case 1 was forced with a steady coastal flow by imposing a volume transport of 0.25 Sv at the model's western boundary (Cape Lisburne), but with zero surface heat and salt fluxes. Case 2 was forced with the 20-day averaged salt and heat fluxes and steady coastal flow. Case 3 included the mean surface fluxes but the coastal flow transport was reduced to a very small value (0.0025 Sv). In case 4 the mean surface fluxes were imposed but the coastal flow was allowed to vary in time.

Cases 5 through 7 fall in the second category and were designed to evaluate the effects of weaker and more rapidly changing polynyas on the stratification, circulation, and salt generation in the study region. Case 5 was forced with time-variant (January 28-February 28, 1997) surface fluxes and time-variant coastal flow. In case 6 the coastal flow transport was reduced to a minimum (0.0025 Sv). Finally, case 7 was forced with time-variant surface fluxes and coastal flow as in case 5, but the surface ice-water stresses were also imposed to evaluate the impact of ice drift momentum transfer on the water properties.

4.1. Mean Salt Flux Forcing Experiments

The effects of different forcing scenarios on the salt distribution and circulation for the first category of experiments (cases 1 through 4) are shown in Figures 6 and 7. Figure 6 shows the 32-day time series of the total salt increment for the four numerical experiments (cases 1 through 4). The experiment forced by coastal flow without surface fluxes (case 1) shows that there was negligible variability in salt content when compared with the other 3 experiments, which were forced with heat and salt surface fluxes. The amount of salt accumulated within the polynya generation area is proportional to the intensity and steadiness of the coastal current. The experiment forced with a steady coastal current yielded the least salt accumulation at the end of the 32 days of simulation. The experiment forced with a very weak coastal current yielded the highest salt accumualtion, while the experiment forced with a time-variant coastal flow produces salt amounts lying between the two extreme cases. Figure 7 shows the salinity and currents at 20 meters for the four different numerical experiments after 30 days of simulation. Only a subset (166°W-156°W, 69.5°N-72°N) of the grid domain, which contains the brine generation area and nearby areas, is shown. The white rectangle delimits the control volume for the calculation of the salt production budget. The location of Barrow Canyon is represented by the 40- and 50-meter isobaths (thick black lines). The 20-day (December 17, 1996 to January 6, 1997) averaged salt production from the two strongest events occurring during that period is 380×10^9 kg.

For case 1 (steady coastal flow and no surface fluxes) the salinity is horizontally homogeneous and there is relatively negligible change in the salt content within the control volume. In case 2 (steady coastal flow and 20-day mean surface fluxes) the horizontal salinity stratification is much stronger, reflecting the salt production inside the polynya. Strong salt advection is evident in the southern flank of Barrow Canyon, just offshore of Point Barrow, judging from the swift (30-40 cm/s) and narrow (50 km) coastal current associated with a downstream gradient in salinity. A cyclonic recirculation is generated east of 160°W and north of the swift coastal current. This recirculation seems to be bathymetrically steered by the canyon topography and is a result of entrainment of offshore canyon water into the narrow and swift coastal flow. Note that some surface freshwater makes its way into the control volume at the western boundary carried by the strong coastal jet. The

total salt retained in the control volume for this experiment after 20 days of simulation is 213×10^9 kg. Thus, 167×10^9 kg (about 44% of the polynya's salt production) were exported by the coastal current. In case 3, for which the coastal current was replaced by a very weak flow, the retention of salt within the control volume is much larger (331×10^9 kg). The salt export, 49×10^9 kg, is realized by a combination of the weak and localized downcanyon gravitational flow ($\leq$ 10 cm/s) generated by the salinity gradient along the coast near Point Barrow, and lateral diffusion. When the time-variant coastal flow is used (case 4), the salt retention in the control volume is about 26% larger (268×10^9 kg) than the steady coastal flow experiment (case 2). The total salt exported by advection ($380-268\times10^9$ kg) after 20 days of simulation is 112×10^9 kg, about 30% of the salt generated by the polynya for the same time period. This result emphasizes the need for realistic time-variant forcing to more accurately assess the salt budget and dense water transport. The difference in salt retention between case 2 and case 4 is most likely due to non-linear interactions of momentum, salt conservation, and topography. Although the majority of the salt produced by polynyas is exported via the strong jet off of Point Barrow, relatively small amounts of salt escape the control volume via the northern boundary towards the Chukchi Sea via gravitational circulation and horizontal diffusion. This is clearly shown in Figure 6 (cases 2, 3, and 4) by the tongue-like shape of the isohalines protruding out of the domain. As shown in case 3, there is also salt transport via the gravitational current generated by the salinity gradient in the vicinity of Point Barrow. The combined effect of gravitational circulation and diffusion accounts for 13% of the salt exported in 20 days. The other mechanism for transporting salt from the production area offshore of the Barrow Canyon region (17% of the total salt produced) is the strong salt advection resulting from the swift coastal current originating from the Bering Strait throughflow.

All numerical experiments were conducted with initial temperature and salinity stratifications based on fall CTD transects [*Signorini et al.*, 1997]. The initial stratification is allowed to change in the model under the influence of surface heat and salt fluxes, and diffusion-advection processes computed by the heat and salt conservation equations. We will now proceed to analyze the impact of the polynya salt production on the temperature and salinity stratification, focussing on the three cross-canyon transects shown in Figures 1 and 4. Figures 8 and 9 show the temperature and salinity stratification along those three transects at time equal zero (left column) and after 30 days of simulation (right column), forced with 20-day averaged heat and salt fluxes at the surface and steady coastal flow (case 2). The shallowest (westernmost) transect is plotted at the top of the figures and the deepest (easternmost) transect is plotted at the bottom of the figures. Both salinity and temperature initial stratifications are horizontally weak but have a significant vertical gradient. The mixed layer homogeneity is apparent down to about 30 meters in both salinity and temperature fields (-1.66 °C and 30.5 psu). There is a relatively sharp halocline below the mixed layer and a homogeneous salinity sublayer between 75 and 100 meters. The mixeed layer water is at freezing temperatures throughout. There is a sharp vertical temperature gradient at 70 meters. These initial conditions are representative of the fall season in the Barrow Canyon region [*Münchow and Carmack*, 1997]. Note the significant change in the salinity and temperature distributions at 30 days when compared to initial conditions. In the shallowest transect the halocline is eroded by the convective mixing due to the dense water formation in the polynya, and the strong bottom mixing due to the nearshore (southeast side of the canyon) coastal current. Below 40 meters (bottom of the canyon) there is vertical stratification in the salinity and temperature fields where vertical mixing is much weaker. The influence of the saltier (30.6 to 30.8 psu) and relatively colder (-1.68 °C) water generated in the polynya region is evident in the top 30 meters by a vertically homogeneous layer extending 350 to 400 km offshore. For the other two transects further downstream the offshore extent of the polynya decreases to 300 and 150 km, respectively, and the mixing depth becomes shallower (25 meters) due to the reduced salt production. There is a strong horizontal gradient of temperature and salinity below 40 meters, and at a distance of less than 100 km offshore, resulting from the baroclinic response of the density field to the strong coastal flow. It is within this 100-km coastal boundary that most of the salt exchange between the polynya-driven salt generation area and the Beaufort Sea shelf break takes place.

A comparison between the salinity and temperature stratifications with and without the polynya heat and salt surface fluxes is shown in Figures 10 and 11. The left side shows the results for case 1 (no surface fluxes) and the right side shows reults for case 2 (with surface fluxes). The effect of the denser wa-

ter injection by the polynya is quite evident by the horizontal temperature and salinity gradients within the mixed layer, which form a front along the edges of the polynya. This contrasts with the results from case 1 where a horizontally uniform mixed layer is present in all three transects. Figures 12 and 13 compare the temperature and salinity stratifications, respectively, between case 3 (left side) and case 2 (right side). These figures are intended to contrast the effects of the polynya-induced heat and salt fluxes with (right side) and without (left side) the presence of the swift coastal current. Note that the coastal current enables deeper mixing near the coast by eroding the shallow halocline (~30 m) all the way to the bottom. Without the coastal current, the colder and saltier water originating from the polynya is limited to spread horizontally by diffusion and weak gravitational advection within the mixed layer (upper 30 meters). This mechanism contrasts with the Arctic halocline ventilation on the Mackenzie Shelf, which occurs during some winters in response to wind-driven upwelling combined with convection induced by the salt expelled from growing sea ice. The water overlying Mackenzie shelf in the southeastern Beaufort Sea becomes quite saline (33-35 psu) and at freezing temperature throughout [*Melling*, 1993]. The model-predicted denser water produced on the shelf in the vicinity of Barrow Canyon during the winter of 1996/1997 was much less saline (30.6 to 30.8 psu) and it was not dense enough to ventilate the Arctic halocline. The question still remains on whether more intense polynyas that may occur on the Chukchi Shelf upstream of Barrow Canyon are capable of ventilating the Arctic halocline. *Cavalieri and Martin*, [1994], based on nine years (1978-1986) of data, suggest that dense water formation from polynyas in the vicinity of Barrow Canyon may ventilate the Arctic halocline when the pre-polynya ambient surface salinity reaches 32 psu. With this ambient salinity, it takes approximately 4 meters of ice growth to bring the water column (~50 m) to a salinity of 34 psu and ventilate the halocline layer. However, these extreme salinity values are not very common in the surface waters upstream of Barrow Canyon (Point Lay to Point Barrow).

4.2. Time-Variant Salt Flux Forcing Experiments

The effects of different forcing scenarios on the salt distribution and circulation for the second category of experiments (cases 5, 6, and 7) are shown in Figures 14 and 15. Figure 14 shows the time series of total salt accumulated within the control volume for the time period of January 28 - February 28, 1997, during which a fast evolving polynya occurred. The three experiments shown are all forced by time-variant surface fluxes but differ in the way the coastal flow and surface stress are applied to the model. Case 5 was forced with time-variant coastal flow, case 6 was forced with a weak and steady flow, and case 7 was forced by both time-variant coastal flow and ice-water stress. The total polynya salt production for this time period was 223×10^9 kg. The total salt accumulated within the control volume after 32 days of simulation for cases 5, 6, and 7 are, respectively, 92×10^9 kg, 155×10^9 kg, and 96×10^9 kg. Therefore, 131×10^9 kg of salt are exported in case 5, 68×10^9 kg in case 6, and 127×10^9 kg in case 7. The largest salt export, 59% of the polynya production, occurs in case 5 where salt advection is larger because of the effect of the time-variant coastal flow. The smallest salt export, 31% of the polynya production, occurs in case 6 because the coastal flow was reduced to a minimum (0.0025 Sv). The salt export mechanisms in this case are mainly lateral diffusion and gravitational flow. In case 7, where the forcing includes time-variant coastal current and ice-water stress, the salt export is slightly less than in case 5 (57% of the polynya production) resulting from a reduction of the coastal current speed due to the ice-water drag forces.

Figure 15 shows time series of coastal flow transport, surface salt flux generated by the polynya, and net salt change within the control volume due to the combine effects of salt expelled by ice growth and salt exported by lateral advection and diffusion. The net salt change time series are shown for cases 5, 6, and 7. There were two events during which the coastal flow transport was relatively high ($\geq$0.2 Sv) and the surface salt flux was very low. These were: February 1 and February 10, 1997. These events led the peak of salt draining, shown by the throughs in the net salt change time series. There were two peak polynya activity events during which the coastal flow transport was relatively low, one on January 30 and one centered on February 4. These events were followed by peaks of net salt change after 1 to 2 days, indicating the approximate advective time scale of polynya-generated salt export from the shelf during weak polynya activity. The time scale response for large salt injections from polynyas associated with very weak coastal flow (case 6) is much more rapid (order of hours) judging from the fast response shown

for the February 10-18 event (the maximum salt injection from the polynya for the January 28 - February 28 time period).

The depth- (surface to 30 meters) and time- (30 days) averaged mixed-layer salinity and currents for cases 5 and 7 are shown in Figure 16. A comparison of case 5 (Figure 16a, no ice-water stress) with case 7 (Figure 16c, with ice-water stress) reveals that the inclusion of the ice-water stress in the model forcing results in the widening of the coastal flow and an overall reduction of the current speeds. Also note that the cyclonic flow in the eastern side of the control volume shown in case 5 is dampened by the surface ice stress in case 7 (Figure 16c). Figure 16b shows the mean ice drift vectors and salt production for the entire simulation period. The mean ice drift ($\sim$ 3-4 cm/s) is west-northwestward, mainly against the eastward flowing coastal current. The ice motion effect on the circulation is twofold: it reduces the surface flow by ice-water drag, and it widens the coastal current due to offshore Ekman transport. The effect in the velocity and salinity transects across Barrow Canyon is shown in Figures 17 and 18. The transects are shown on the left side for case 5 (no ice stress), and on the right for case 7 (with ice stress). Note that the coastal current (Figure 17) is much swifter and narrow ($\sim$ 50 km) in case 5 than in case 7 where the width of the current is about 100 to 150 km. In addition, the return flow (negative velocities) in case 7 is very weak for the top and middle transects, and absent in the bottom transect. The salinity transects in Figure 18 show that the spreading of the salt produced by the polynya is confined to the mixed layer. Also, the offshore extent of the polynya front, indicated by the 30.3 isohaline in the top and middle transects, is wider in case 7 than in case 5. The polynya influence is stronger and wider further upstream (Figure 16) where surface salinity is greater than 30.5 psu (transects not shown).

Figure 19 shows the mean salinity distribution and a three dimensional rendition of bottom topography within the domain of the control volume box. The salt exchange pathways are shown by the large arrows. The polynya salt production enters the control volume via the surface flux (1). Most of the exported salt leaves the control volume via strong advection imparted by the swift flow at the southern flank of Barrow Canyon (4). The lateral exchange via the west (2) and northern boundaries (3) is relatively much smaller. The mixing depth is a function of the intensity of the polynya salt production and the strength of the coastal current. The salt exchange from weak polynyas is confined to the mixed layer while salt from strong polynyas combined with swift coastal current mixes all the way to the bottom of the canyon near the coast. For case 7, for which the forcing fields are the most realistic (time-variant surface salt flux, coastal current, and surface ice-water stress), the total salt accumulated for the 32-day simulation (January 28 - February 28, 1997) within the shelf region delimited by the control volume is 96×10^9 kg. The total salt production by the polynya for the same time period is 223×10^9 kg. The difference of 127×10^9 kg is primarily exported via Barrow Canyon by the coastal current.

5. Summary and Conclusions

Numerical experiments were conducted using a high resolution (1 to 5 km) numerical model with realistic topography, ambient stratification, and ambient flow for the Chukchi and Beaufort Seas. A total of seven numerical experiments were conducted to determine the effects of different combinations of model forcing on the salt transport, stratification, and circulation. The experiments can be divided into two major categories, those conducted with time-averaged surface flux forcing, and those conducted with time-variant flux forcing. Several forcing combinations were imposed under each of these two major categories. One experiment also included surface momentum forcing from ice-water stresses.

Results from this study show that the ambient stratification plays a major role in controlling the spreading of salt produced by the polynyas. Previous modeling experiments have shown that with strong stratification dense water is transported across the shelfbreak at intermediate depths, whereas with weak stratification dense water moves downslope and is trapped near the bottom (*Gawarkiewicz*, [2000]). The summer-fall melting produces a shallow ($\sim$30 m) halocline in the Chukchi Sea which provides a barrier layer for the vertical mixing of polynya-generated saltier water in the winter. During the polynya events of 1996/1997, the brine rejection did not produce water densities sufficiently high to erode the shallow halocline barrier layer. The only exception were the shallow ($\leq$ 30 m) areas of the Chukchi Sea where bottom boundary turbulence produces intense mixing, and the coastal boundary layer where lateral shear from the swift Alaska coastal current entrains and mixes the saltier water. The coastal current promotes 40 to 60% of the total salt exported offshore via Bar-

row Canyon. The inclusion of an ice-water boundary layer in the model broadens and slightly weakens the coastal current, thus reducing the salt export from 59% to 57% of the total polynya salt production in 32 days.

One question that still remains is whether Chukchi Sea polynyas in the vicinity of Barrow Canyon can produce enough salt to ventilate the Arctic halocline during some winters. As noted earlier, *Cavalieri and Martin* [1994] argued that an ambient surface salinity of about 32 psu and approximately 4 meters of ice growth would be required to bring a 50 meter water column to a salinity of 34 psu. Under these conditions, the water formed by the polynya is sufficiently dense to ventilate the Arctic halocline. These conditions were not encountered during the winter of 1996/1997. As future work, we propose to extend the regional domain to include a larger number of polynya areas and multi-year events to capture a more complete range of forcing conditions for the model. For example, during the winter of 1991/1992 daily salt rejection from polynyas in the vicinity of Barrow Canyon peaked at $\sim$40-50$\times 10^9$ kg (*Weingartner et al.*, 1998), a value five times larger than the peak daily salt rejection during the winter of 1996/1997. These large interannual changes in polynya activity are consistent with the recent study of *Winsor and Björk* [2000].

One particular area of interest not covered by this study is the Mackenzie shelf region. During some winters, the water overlying Mackenzie shelf in the southeastern Beaufort Sea becomes quite saline (33-35 psu) and at freezing temperature throughout as a result of salt expelled from growing sea ice [*Melling*, 1993]. Therefore, areas such as the Mackenzie shelf are likely candidates for further numerical studies of the oceanic response to dense water formation and an evaluation ot its impact on the Arctic halocline.

Acknowledgments. We are thankful to Jodi Humphreys of SAIC General Sciences Corporation and X. Zhang of Raytheon ITSS for providing the heat and salt fluxes derived from SSM/I data. We are also thankful to A. Liu of the NASA-GSFC Laboratory for Hydrospheric Processes and Y. Zhao of CAELUM for providing the ice drift data derived from SSM/I and NSCAT data. This work was sponsored by the Office of Naval Research under contract No. N00014-98-C-0022 MOD P00003.

References

Aagaard, K., L. K. Coachman, and E. C. Carmack, On the halocline of the Arctic Ocean, *Deep Sea Res., 29,* 529-545, 1981.

Aagaard, K., A. T. Roach, and J. D. Schumacher, On the wind-driven variability of the flow through Bering Strait, *J. Geophys. Res., 90,* 7213-7221, 1985.

Aagaard, K., and E. Carmac, The Arctic Ocean and climate: A perspective, in *The Polar Oceans and Their Role in Shaping the Global Environment, Geophys. Mono. Ser.*, vol. 85, edited by O. M. Johannessen, R. D. Muench, and J. E. Overland, pp. 5-20, AGU, Washington D. C., 1994.

Cavalieri, D. J., P. Gloersen, and W. J. Campbell, Determination of sea ice parameters with the Nimbus 7 SMMR, *J. Geophys. Res., 89,* 5355-5369, 1984.

Cavalieri, D. J., and S. Martin, The contribution of Alaskan, Siberian, and Canadian coastal polynyas to the cold halocline layer of the Arctic Ocean, *J. Geophys. Res., 99,* 18,343-18,362, 1994.

Chapman, D. C., and G. Gawarkiewicz, Offshore transport of dense shelf water in the presence of a submarine canyon, *J. Geophys. Res., 100,* 13,373-13,387, 1995.

Coachman, L. K., and C. A. Barnes, The contribution of Bering Sea water to the Arctic Ocean, *Arctic, 14,* 147-161, 1961.

Coachman, L. K., and K. Aagaard, On the water exchange through Bering Strait, *Limnol. Oceanogr., 11,* 44-59, 1966.

Coachman, L. K., K. Aagaard, and R. B. Tripp, *Bering Strait: The Regional Physical Oceanography,* 172 pp., University of Washington Press, Seattle, 1975.

Coachman, L. K., and K. Aagaard, Transports through Bering Strait: Annual and interannual variability, *J. Geophys. Res., 93,* 15,535-15,539, 1988.

Gloersen, P., and D. J. Cavalieri, Reduction of weather effects in the calculation of sea ice concentration from microwave radiances, *J. Geophys. Res., 91,* 3913-3919, 1986.

Gawarkiewicz, G., and D. C. Chapman, A numerical study of dense water formation and transport on a shallow, sloping continental shelf, *J. Geophys. Res., 100,* 4489-4507, 1995.

Gawarkiewicz, G., Effects of ambient stratification and shelfbreak topography on offshore transport of dense

water on continental shelves, *J. Geophys. Res., 105,* 3307-3324, 2000.

Junkclaus, J. H. , and J. O. Backhaus, Application of a transient reduced gravity plume model to Denmark Strait Overflow, *J. Geophys. Res., 99,* 12,375-12,396, 1994.

Junkclaus, J. H. , J. O. Backhaus, H. Fohrmann, Outflow of dense water from the Storfjord in Svalbard: A numerical model study, *J. Geophys. Res., 100,* 24,719-24,728, 1995.

Kalnay, E., et al., The NCEP/NCAR 40-year reanalysis project, *Bull. Amer. Met. Soc., 77,* 437-471, 1996.

Killworth, P. D., and J. M. Smith, A one-and-a-half dimensional model for the Arctic halocline, *Deep Sea Res., 31,* 271-293, 1984.

Liu, A.K. and D. J. Cavalieri, On sea ice drift from the wavelet analysis of the Defense Meteorological Satellite Program (DMSP) Special Sensor Microwave Imager (SSM/I) Data, *Int. J. Remote Sensing, 19,* 1415-1423, 1998.

Liu, A. K., Y. Zhao, and S. Y. Wu, Arctic sea ice drift from wavelet analysis of NSCAT and special sensor microwave imager data, *J. Geophys. Res., 104,* 11,529-11,538, 1999.

Martin, S., and P. Kaufman, A field and laboratory study of wave damping by grease ice, *J. Glaciol., 27,* 283-314, 1981.

Melling, H., The formation of a haline shelf front in wintertime in an ice-covered arctic sea, *Cont. Shelf Res., 13,* 1123-1147, 1993.

Millero, F.L., Freezing point of sea water. Eighth report of the Joint Panel of Oceanographic Tables and Standards, Appendix 6, *UNESCO Tech. Pap. Mar. Sci., 28,* 29-31, 1975.

Münchow, A., and E. C. Carmack, Synoptic flow and density observations near an Arctic shelf break, *J. Phys. Oceanogr., 27,* 1402-1419, 1997.

Pacanowski, R. C., and G. H. Philander, Parameterization of vertical mixing in numerical models of tropical oceans, *J. Phys. Oceanogr., 11,* 1443-1451, 1981.

Pease, C. H., The size of wind-driven coastal polynyas, *J. Geophys. Res., 92,* 7049-7059, 1987.

Signorini, S. R., A. Münchow, and D. Haidvogel, Flow dynamics of a wide Arctic canyon, *J. Geophys. Res., 102,* 18,661-18,680, 1997.

Song Y. and D. Haidvogel, A Semi-implicit Ocean Circulation Model Using a Generalized Topography-Following Coordinate System, *J. of Comp. Phys. , 115,* 228-244, 1994.

Stigebrandt, A., The North Pacific: A global scale estuary, *J. Phys. Oceanogr., 14,* 464-470, 1984.

Weingartner, T. J., D. J. Cavalieri, K. Aagard, and Y. Sasaki, Circulation, dense water formation, and outflow on the northeast Chukchi shelf, *J. Geophys. Res., 103,* 7647-7661, 1998.

Winsor, P., and G. Björk, Polynya activity in the Arctic Ocean from 1958 to 1997, *J. Geophys. Res., 105,* 8789-8803, 2000.

D. Cavalieri, Code 971, Laboratory for Hydrospheric Processes, NASA Goddard Space Flight Center, Greenbelt, MD 20771.

S. R. Signorini, SAIC General Sciences Corporation, 4600 Powder Mill Road Beltsville, Maryland 20705-2675 (e-mail: sergio@bluefin.gsfc.nasa.gov)

This preprint was prepared with AGU's LaTeX macros v4. File paper'polynya'rev1 formatted June 1, 2000.

Figure 1. Map of the study region showing the model grid and topography. The dots within the grid domain represent every second grid point. The three thick lines show the location of the Barrow Canyon transects analyzed in this study.

Figure 2. Time series of daily open water amounts for the entire study region.

Figure 3. SSM/I-derived salt fluxes (in Gg/d) for days 43 through 50 (February 12-19, 1997). Note that the strongest event occurs on February 17. The daily ice drift is shown by the superimposed black vectors.

Figure 4. Mean salt production (10^6 kg/d) for polynya events during the period of December 17, 1996 through January 6, 1997. The white line delimits the control volume for total salt variability. The three thick black lines show the location of the Barrow Canyon transects analyzed in this study.

Figure 5. Time series of daily east and north wind components in Bering Strait, wind component towards 192°T in Bering Strait, derived Bering Strait volume transport, and derived Cape Lisburne volume transport.

Figure 6. Total salt increment, in 10^9 kg, within the control volume shown in Figure 4 for four different numerical experiments (cases 1, 2, 3, and 4). Case 1 is the baseline experiment (no surface flux with coastal flow forcing) which shows a relatively small salt change. Case 2 is forced by 20-day averaged salt flux and steady 0.25 sv coastal flow. Case 3 is forced by 20-day averaged salt flux with weak coastal flow. Case 4 is forced by 20-day averaged salt flux and time-variant coastal flow (e. g., wind modulated).

Figure 7. Salinity and currents at 20 meters from four different numerical experiments after 30 days of simulation. The white rectangle delimits the control volume for the calculation of the salt production budget. The 40 and 50 meter isobaths are represented by the thick black lines. The top left plate shows results from case 1 (no surface fluxes with steady coastal flow), the top right plate shows results from case 2 (surface fluxes with steady coastal flow), the bottom left plate shows results from case 3 (surface fluxes with very weak coastal flow), and the bottom right plate shows results from case 4 (surface fluxes with time-variant coastal flow).

Figure 8. Initial temperature section (left) and temperature section after 30 days (right) at 3 transects perpendicular to the coast and across the polynya brine generation area. Note that these transects are also perpendicular to Barrow Canyon. The contours are 0.02 for $T \leq -1.6$°C and 0.2 for $T \geq -1.6$°C. These are results from experiment No. 2 (20-day averaged heat and salt fluxes with steady coastal flow).

Figure 9. Initial salinity section (left) and salinity section after 30 days (right) at 3 transects perpendicular to the coast and across the polynya brine generation area. Note that these transects are also perpendicular to Barrow Canyon. The contours are 0.1 for $S \leq 30.7$ psu and 0.2 for $S \geq 30.7$ psu. These are results from experiment No. 2 (20-day averaged heat and salt fluxes with steady coastal flow).

Figure 10. Temperature sections after 30 days from model runs with (case 2, right) and without (case 1, left) heat and salt surface fluxes from polynya. A steady, 0.25 Sverdrup coastal flow is imposed in both runs. Temperatures are shown at 3 transects perpendicular to the coast and across the polynya brine generation area. Note that these transects are also perpendicular to Barrow Canyon. The contours are 0.02 for $T \leq -1.6$°C and 0.2 for $T \geq -1.6$°C.

Figure 11. Salinity sections after 30 days from model runs with (case 2, right) and without (case 1, left) heat and salt surface fluxes from polynya. A steady, 0.25 Sverdrup coastal flow is imposed in both runs. Salinities are shown at 3 transects perpendicular to the coast and across the polynya brine generation area. Note that these transects are also perpendicular to Barrow Canyon. The contours are 0.1 for $S \leq 30.7$ psu and 0.2 for $S \geq 30.7$ psu.

Figure 12. Temperature sections after 30 days from model runs with (case2, right) and without (case 3, left) coastal flow. Heat and salt surface fluxes from polynya are imposed on both cases. Temperatures are shown at 3 transects perpendicular to the coast and across the polynya brine generation area. Note that these transects are also perpendicular to Barrow Canyon. The contours are 0.02 for $T \leq -1.6$°C and 0.2 for $T \geq -1.6$°C.

Figure 13. Salinity sections after 30 days from model runs with (case2, right) and without (case 3, left) coastal flow. Heat and salt surface fluxes from polynya are imposed on both cases. Salinities are shown at 3 transects perpendicular to the coast and across the polynya brine generation area. Note that these transects are also perpendicular to Barrow Canyon. The contours are 0.1 for S $\leq$ 30.7 psu and 0.2 for S $\geq$ 30.7 psu.

Figure 14. Total salt increment, in 10^9 kg, within the control volume shown in Figure 4 for three different numerical experiments (cases 5, 6, and 7). The simulation was conducted for the period of January 28 through February 28, 1997. The total polynya salt production for this time period was 223×10^9 kg. Case 5 was forced by time-variant surface fluxes (salt and heat) and time-variant coastal current. Case 6 was forced by time-variant surface fluxes and a very weak and steady coastal current. The forcing for case 7 was similar to case 5, except that time-variant ice-water stress was also imposed at the surface.

Figure 15. Time series of coastal flow transport, surface salt flux from polynyas, and net salt change due to polynya production and horizontal transport for January 28-February 28, 1997. The net salt change time series are shown for 3 simulations: (1) surface heat/salt flux forcing with coastal flow (case 5); (2) surface heat/salt flux forcing with weak and steady coastal flow (case 6); and (3) surface heat/salt flux forcing, surface ice stress forcing, and coastal flow (case 7). Daily salt/heat fluxes and coastal flow transport are used in these simulations. Daily surface ice stress is also used to force the run for case 7.

Figure 16. Salinity distribution and currents for case 5 (a) and case 7 (c) simulations, and ice drift and salt production (b) for January 28 - February 28, 1997. The white rectangle delimits the control volume for the calculation of the salt production budget. Case 5 is forced with time-variant salt/heat fluxes and coastal flow. Case 7 is forced with time variant salt/heat fluxes, coastal flow, plus ice-ocean surface stress. The ice drift is primarily against the coastal flow, thus reducing its intensity. Note that the cyclonic flow in the eastern side of the control volume shown in case 5 is dampened by the surface ice stress in case 7. Both salinity and currents were depth-(surface to 30 meters) and time-averaged (30 days). The ice drift was averaged over the 30-day period while the salt production is summed over the same time period. Current and ice drift vectors with amplitude $\leq$ 2 cm/s are not plotted.

Figure 17. Thirty-day averaged sections of u-component of velocity from model runs with (case 6, right) and without (case 5, left) surface ice stress. The u-component is shown at 3 transects perpendicular to the coast and across the polynya brine generation area. Note that these transects are also perpendicular to Barrow Canyon. The contour intervals are 1 cm/s for $u \leq 10$ cm/s and 5 cm/s for $u \geq 10$ cm/s.

Figure 18. Thirty-day averaged sections of salinity from model runs with (case 6, right) and without (case 5, left) surface ice stress. The salinity is shown at 3 transects perpendicular to the coast and across the polynya brine generation area. Note that these transects are also perpendicular to Barrow Canyon. The contour intervals are 0.1 for $S \leq 30.7$ psu and 0.2 for $S \geq 30.7$ psu.

Figure 19. Mean salinity distribution and three dimensional rendition of bottom topography within the domain of the control volume box. The salt exchange pathways are shown by the large arrows. The polynya salt production enters the control volume via the surface flux (1). Most of the exported salt leaves the control volume via strong advection imparted by the swift flow at the southern flank of Barrow Canyon (4). The lateral exchange via the west (2) and northern boundaries (3) is relatively much smaller.

Table 1. Layer depth in meters for model grid points at minimum depth (H_{min}=20 m), over the slope (H_{slope}=1010 m), and at maximum depth (H_{max}=2000 m).

Level	s[a]	H_{min}	H_{slope}	H_{max}
25	0.00	0.00	0.00	0.00
24	-0.04	-0.80	-16.21	-31.61
23	-0.08	-1.60	-32.58	-63.56
22	-0.12	-2.40	-49.29	-96.18
21	-0.16	-3.20	-66.51	-129.81
20	-0.20	-4.00	-84.41	-164.82
19	-0.24	-4.80	-103.18	-201.56
18	-0.28	-5.60	-123.02	-240.44
17	-0.32	-6.40	-144.13	-281.86
16	-0.36	-7.20	-166.73	-326.26
15	-0.40	-8.00	-191.05	-374.11
14	-0.44	-8.80	-217.36	-425.93
13	-0.48	-9.60	-245.93	-482.26
12	-0.52	-10.40	-277.05	-543.71
11	-0.56	-11.20	-311.07	-610.93
10	-0.60	-12.00	-348.32	-684.65
9	-0.64	-12.80	-389.22	-765.65
8	-0.68	-13.60	-434.20	-854.79
7	-0.72	-14.40	-483.72	-953.05
6	-0.76	-15.20	-538.33	-1061.46
5	-0.80	-16.00	-598.60	-1181.21
4	-0.84	-16.80	-665.18	-1313.56
3	-0.88	-17.60	-738.78	-1459.96
2	-0.92	-18.40	-820.18	-1621.97
1	-0.96	-19.20	-910.27	-1801.34
0	-1.00	-20.00	-1010.00	-2000.00

[a]Generalized s coordinate (*Song and Haidvogel*, [1994]).

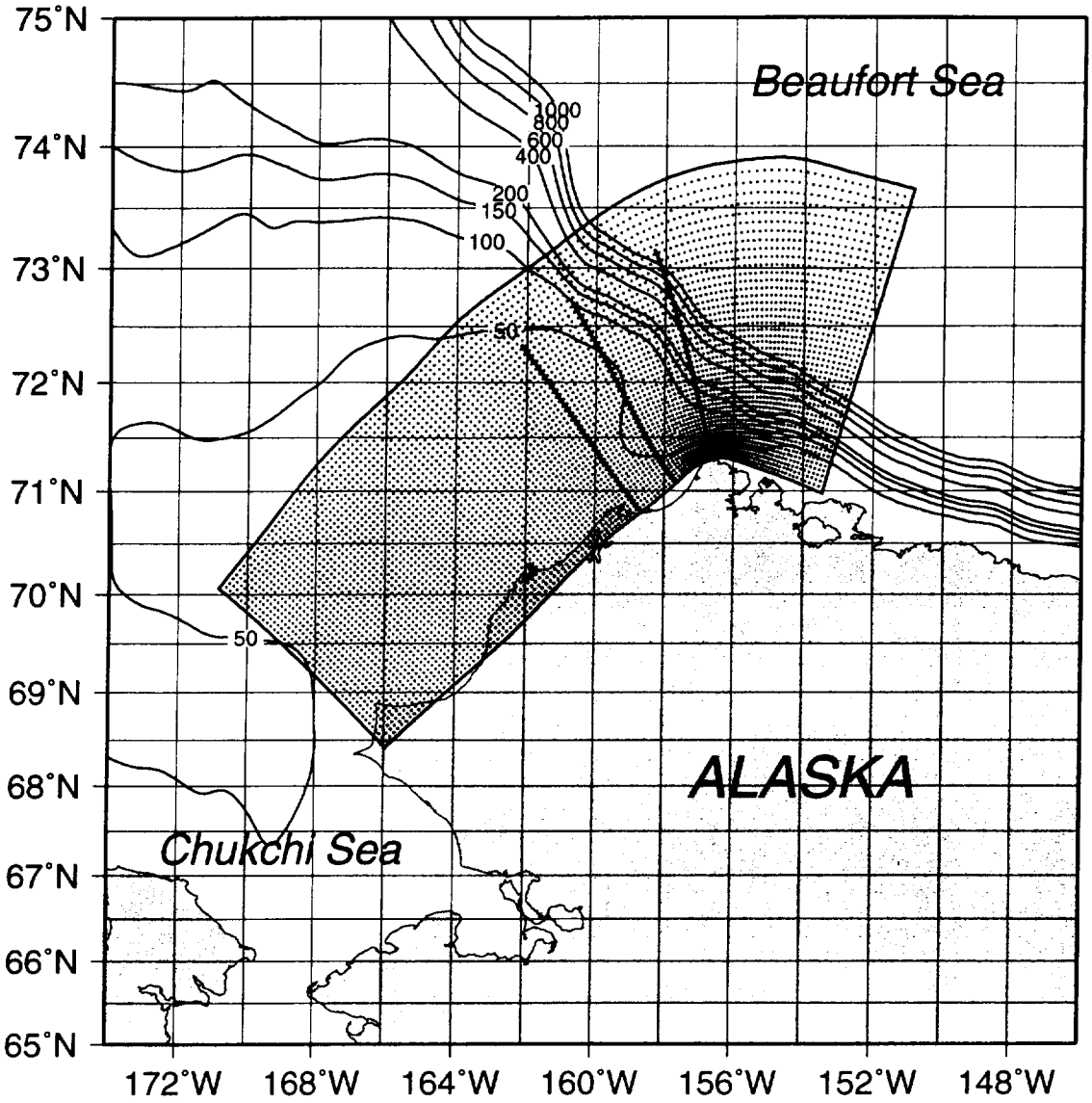

Figure 1. Map of the sudy region showing the model grid and topography. The dots within the grid domain represent every second grid point. The three thick lines show the location of the Barrow Canyon transects analyzed in this study.

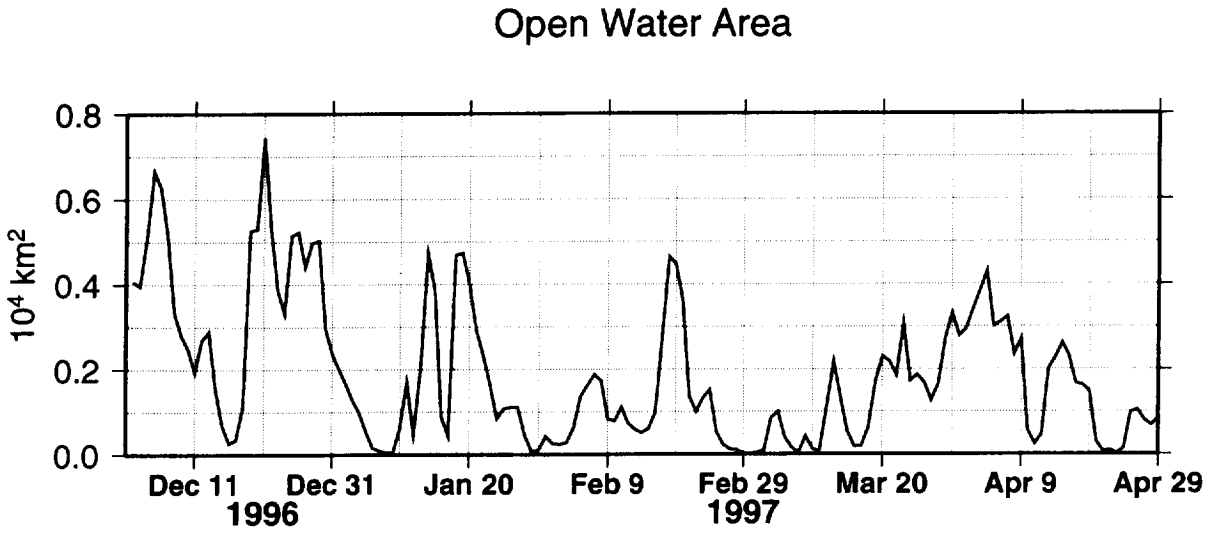

Figure 2. Time series of daily open water amounts for the entire study region after freezeup. The series starts on December 1, 1996, and ends on April 29, 1997.

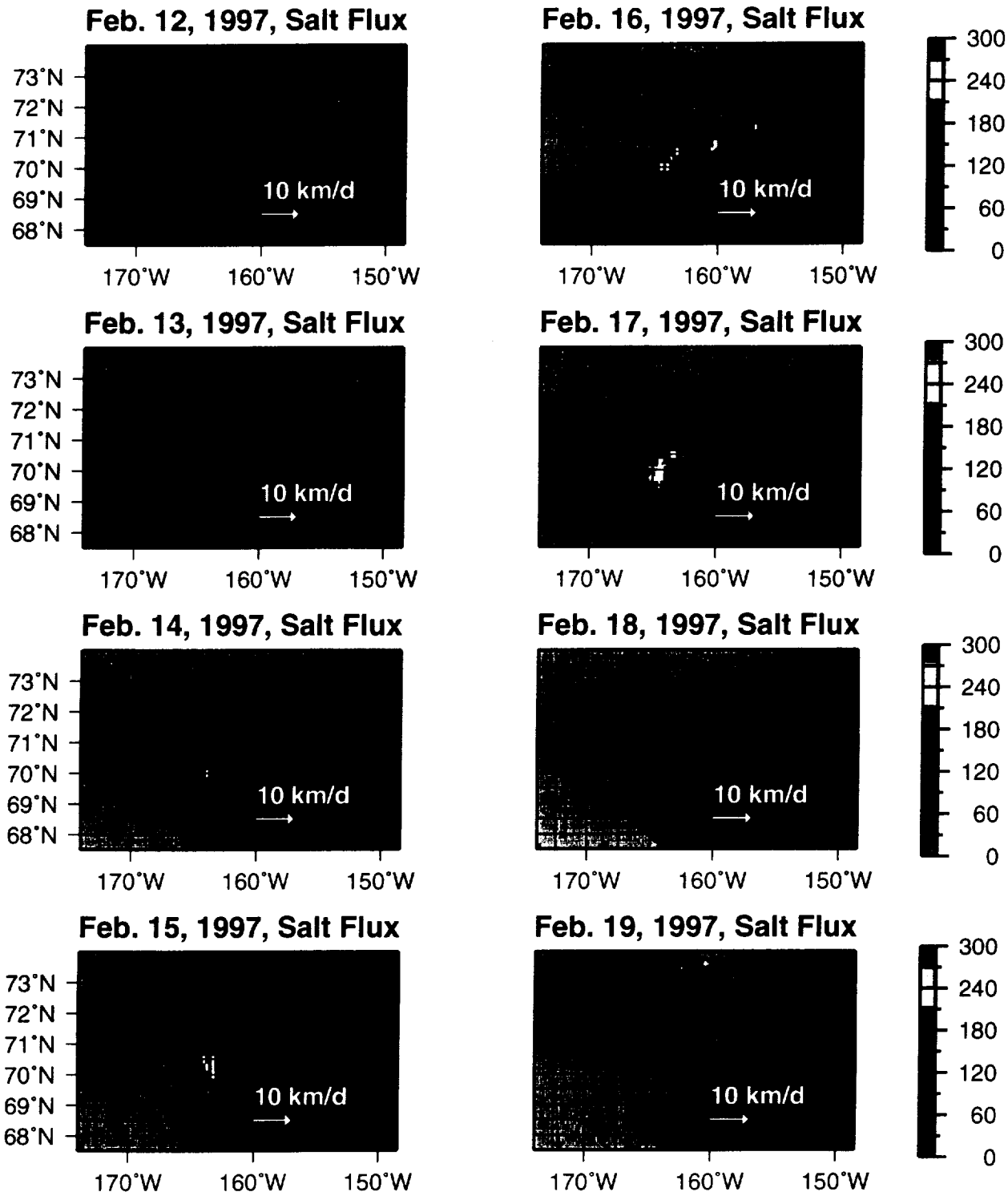

Figure 3. SSM/I-derived salt production (in 10^6 kg/d) for February 12-19, 1997. Note that the strongest event occurs on February 17. The ice drift vectors (in km/d) derived from merged DMSP SSM/I and ADEOS NSCAT data sets are superimposed on the daily salt fluxes.

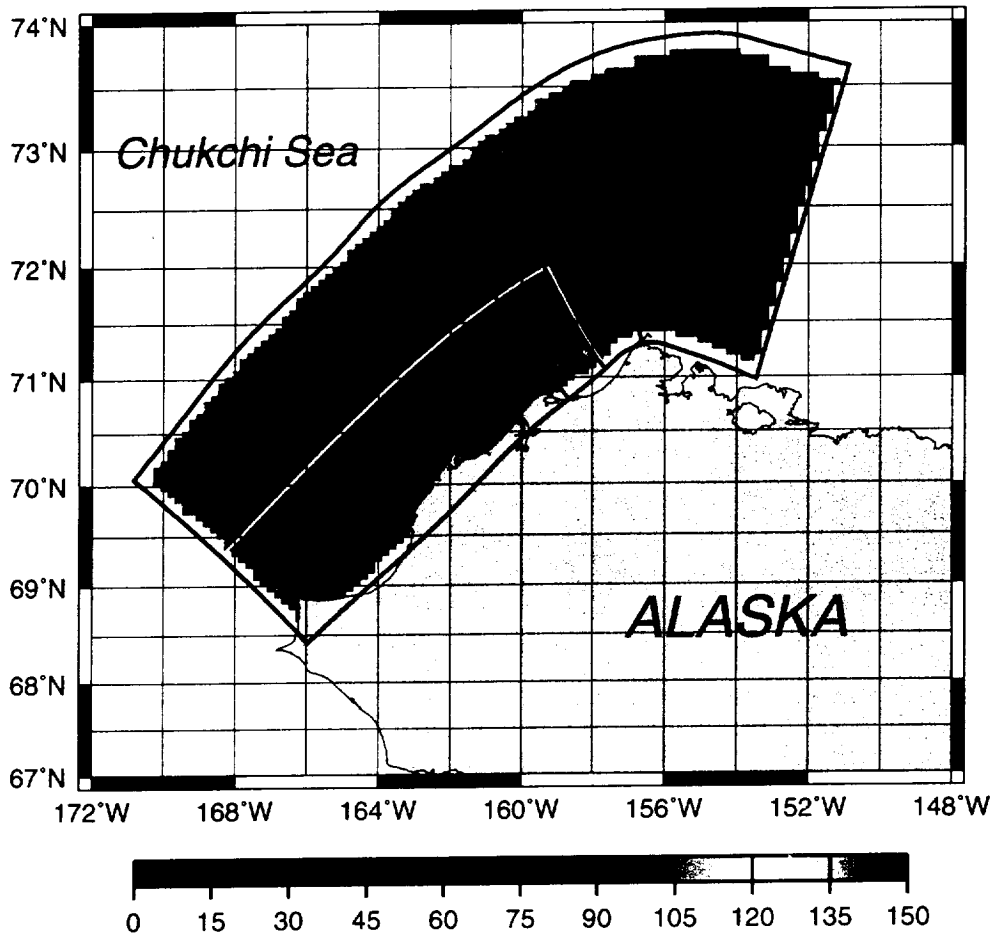

Figure 4. Mean salt production (10^6 kg/d) for polynya events during the period of December 17, 1996 through January 6, 1997. The white line delimits the control volume for total salt variability. The three thick black lines show the location of the Barrow Canyon transects analyzed in this study.

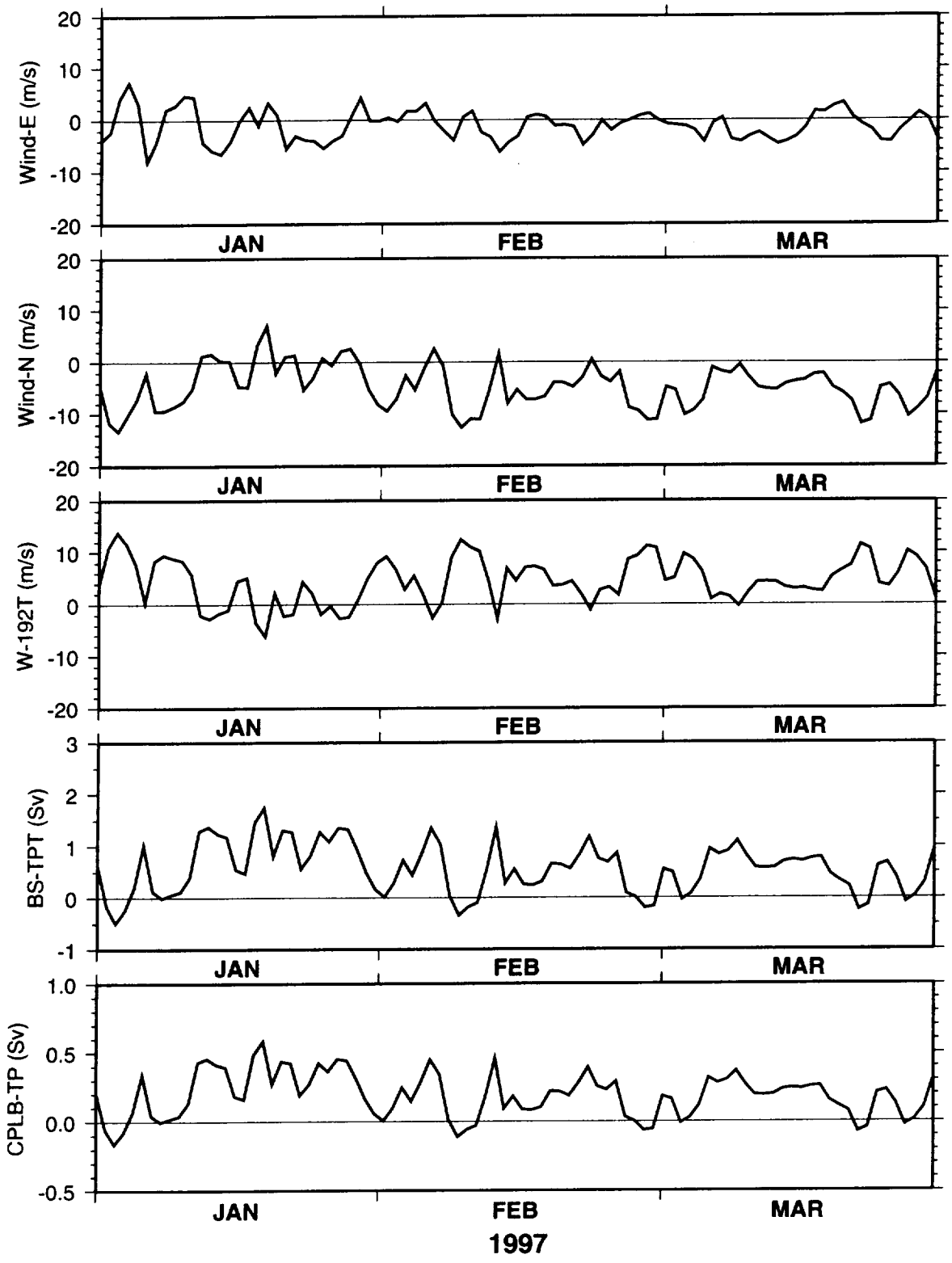

Figure 5. Time series of daily east and north wind components in Bering Strait, wind component towards 192°T in Bering Strait, derived Bering Strait volume transport, and derived Cape Lisburne volume transport.

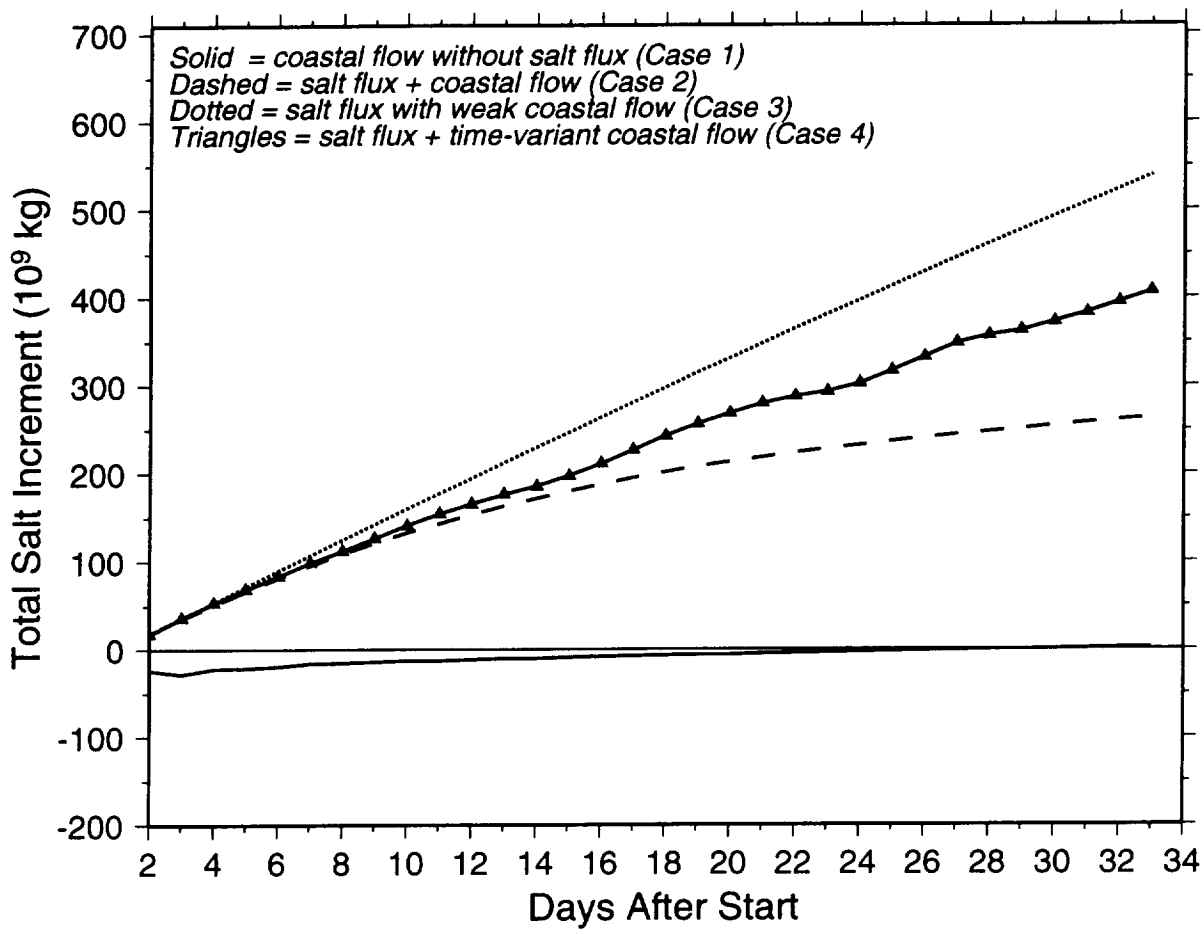

Figure 6. Total salt increment, in 10^9 kg, within the control volume shown in Figure 4 for four different numerical experiments (cases 1, 2, 3, and 4). Case 1 is the baseline experiment (no surface flux with coastal flow forcing) which shows a relatively small salt change. Case 2 is forced by 20-day averaged salt flux and steady 0.25 sv coastal flow. Case 3 is forced by 20-day averaged salt flux with weak coastal flow. Case 4 is forced by 20-day averaged salt flux and time-variant coastal flow (e. g., wind modulated). The total salt stored within the control volume for cases 2, 3, and 4 is 213×10^9 kg, 331×10^9 kg, and 268×10^9 kg, respectively. For case 4, which is forced by the more realistic time-variant coastal current, the total salt exported by advection for the 20-day simulation period is 76×10^9 kg ($380\text{-}268=112\times10^9$ kg). This amounts to 30% of the 380×10^9 kg of salt generated by the polynya in 20 days. The majority of the salt export occurs via Barrow Canyon at its southeastern flank near the coast.

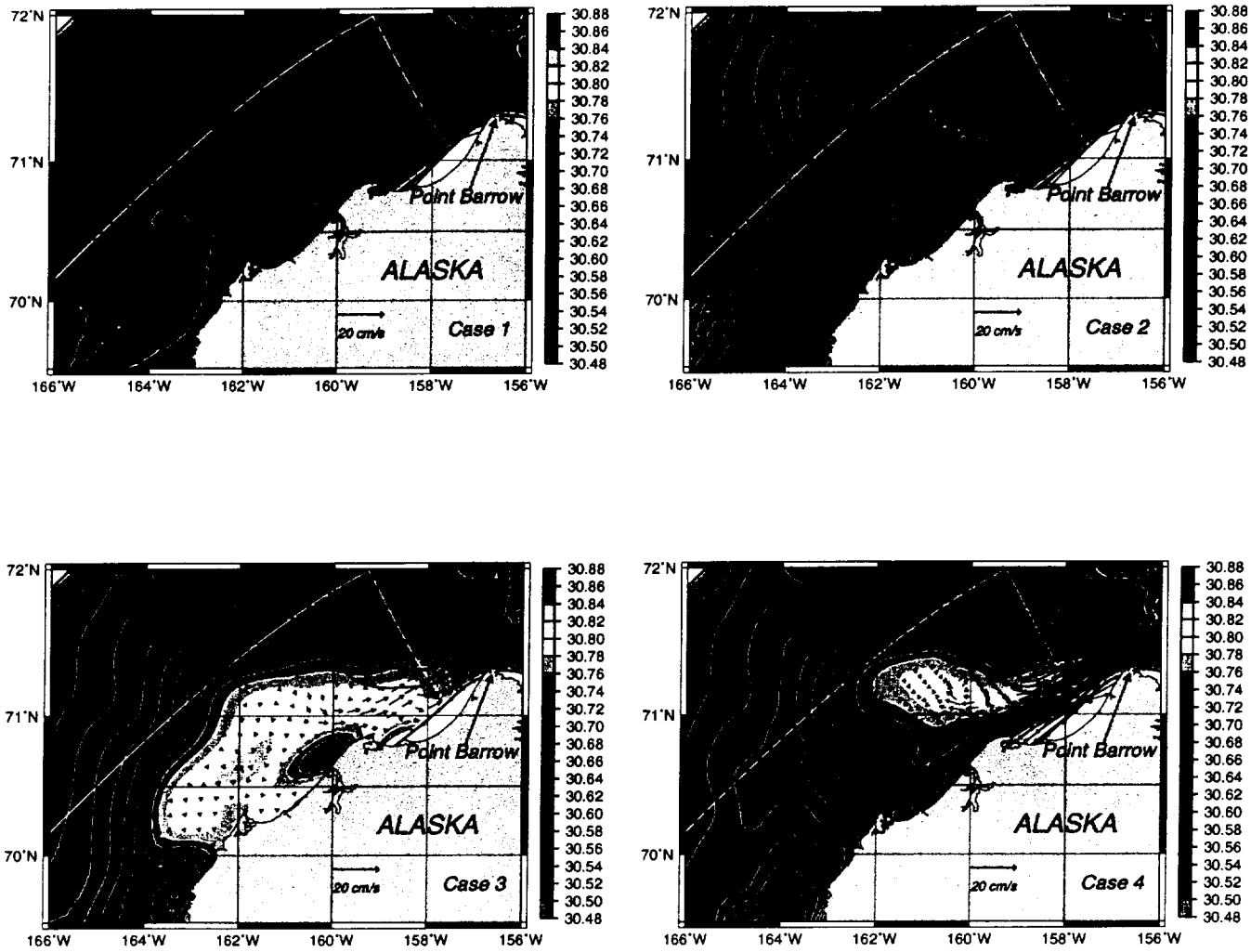

Figure 7. Salinity and currents at 20 meters from four different numerical experiments after 30 days of simulation. The white rectangle delimits the control volume for the calculation of the salt production budget. The 40 and 50 meter isobaths are represented by the thick black lines. The top left plate shows results from case 1 (no surface fluxes with steady coastal flow), the top right plate shows results from case 2 (surface fluxes with steady coastal flow), the bottom left plate shows results from case 3 (surface fluxes with very weak coastal flow), and the bottom right plate shows results from case 4 (surface fluxes with time-variant coastal flow).

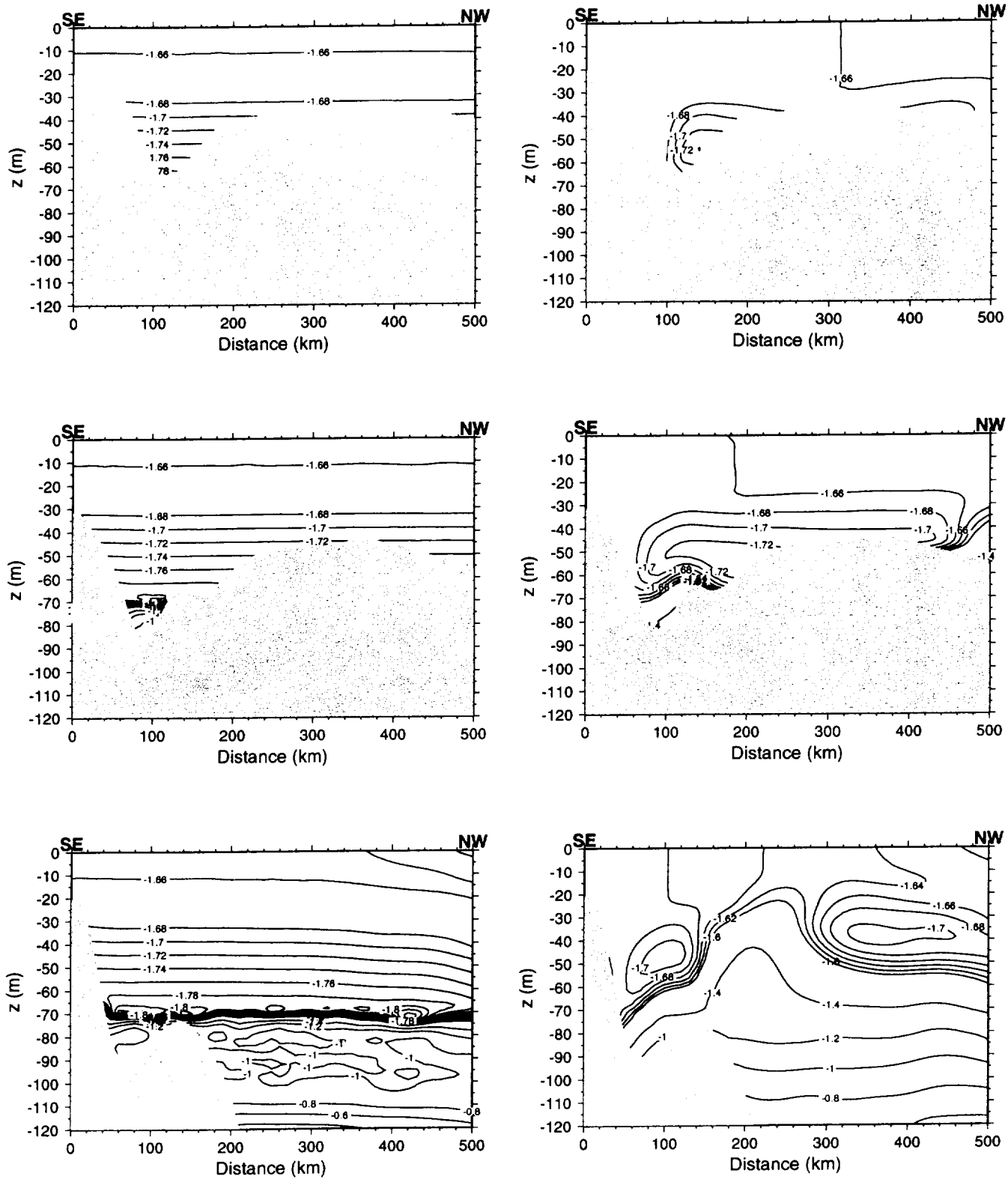

Figure 8. Initial temperature section (left) and temperature section after 30 days (right) at 3 transects perpendicular to the coast and across the polynya brine generation area. Note that these transects are also perpendicular to Barrow Canyon. The contours are 0.02 for T $\leq$ -1.6°C and 0.2 for T $\geq$ -1.6°C. These are results from experiment No. 2 (20-day averaged heat and salt fluxes with steady coastal flow).

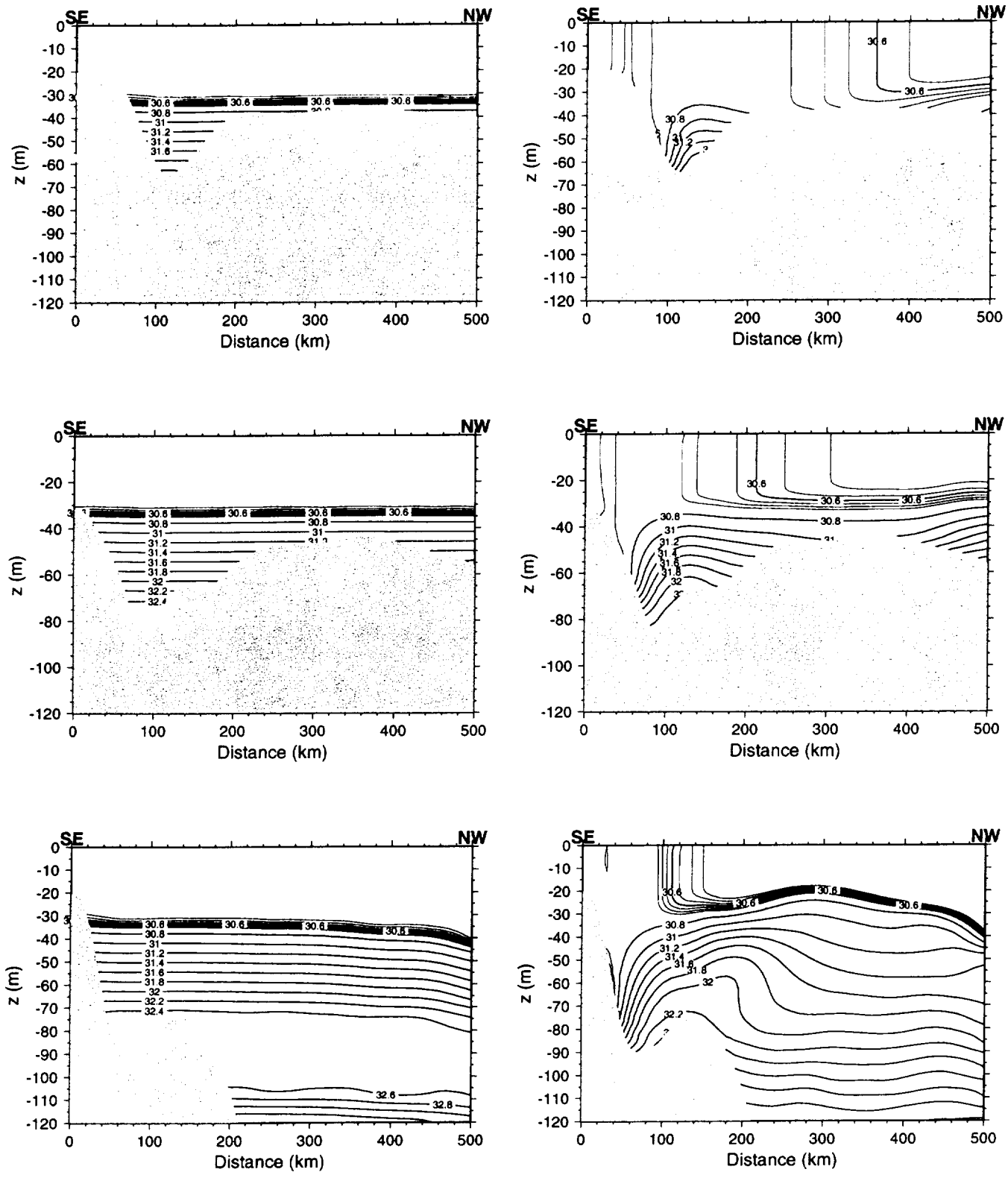

Figure 9. Initial salinity section (left) and salinity section after 30 days (right) at 3 transects perpendicular to the coast and across the polynya brine generation area. Note that these transects are also perpendicular to Barrow Canyon. The contours are 0.1 for $S \leq 30.7$ psu and 0.2 for $S \geq 30.7$ psu. These are results from experiment No. 2 (20-day averaged heat and salt fluxes with steady coastal flow).

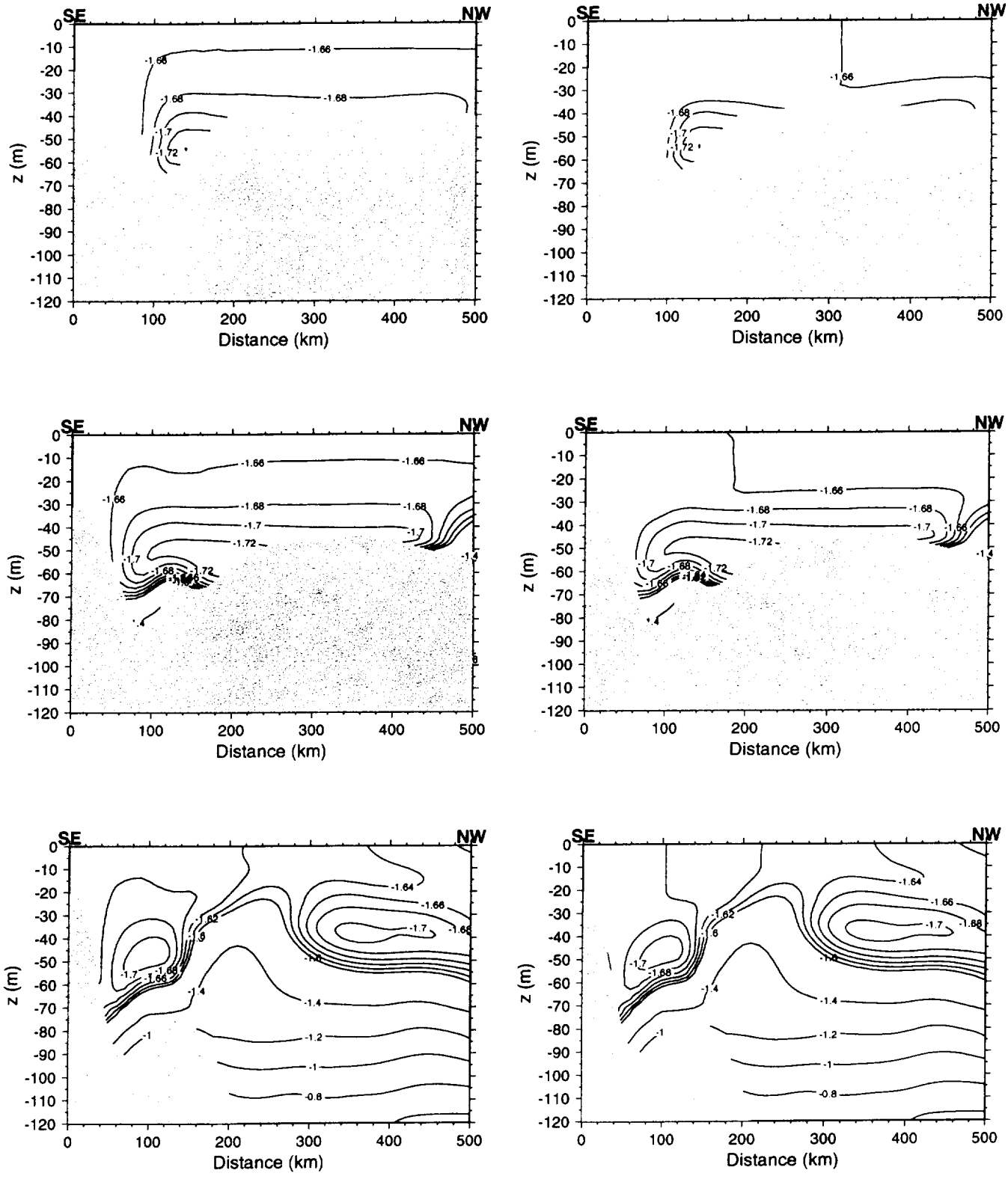

Figure 10. Temperature sections after 30 days from model runs with (case 2, right) and without (case 1, left) heat and salt surface fluxes from polynya. A steady, 0.25 Sverdrup coastal flow is imposed in both runs. Temperatures are shown at 3 transects perpendicular to the coast and across the polynya brine generation area. Note that these transects are also perpendicular to Barrow Canyon. The contours are 0.02 for $T \leq -1.6°C$ and 0.2 for $T \geq -1.6°C$.

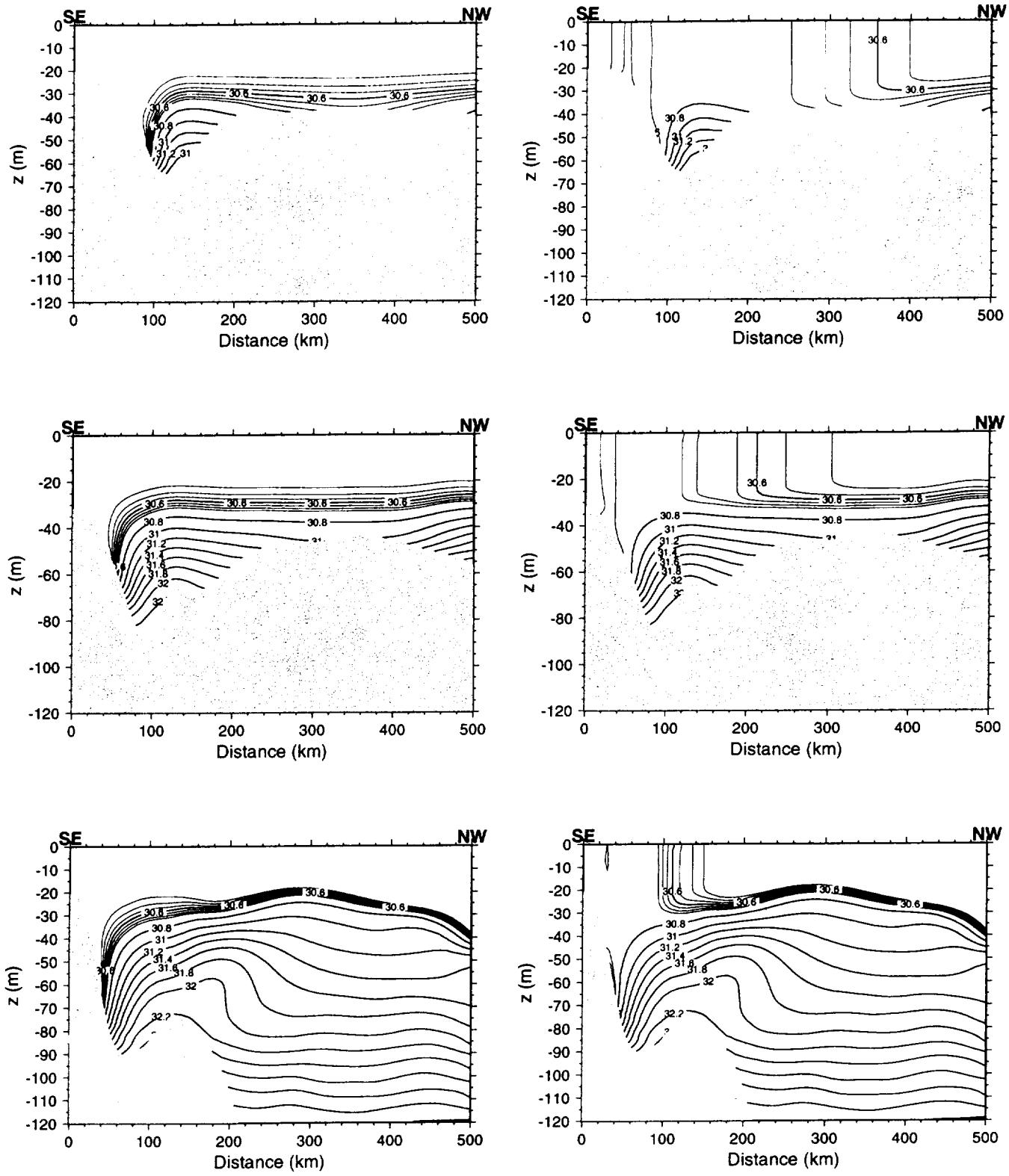

Figure 11. Salinity sections after 30 days from model runs with (case 2, right) and without (case 1, left) heat and salt surface fluxes from polynya. A steady, 0.25 Sverdrup coastal flow is imposed in both runs. Salinities are shown at 3 transects perpendicular to the coast and across the polynya brine generation area. Note that these transects are also perpendicular to Barrow Canyon. The contours are 0.1 for $S \leq 30.7$ psu and 0.2 for $S \geq 30.7$ psu.

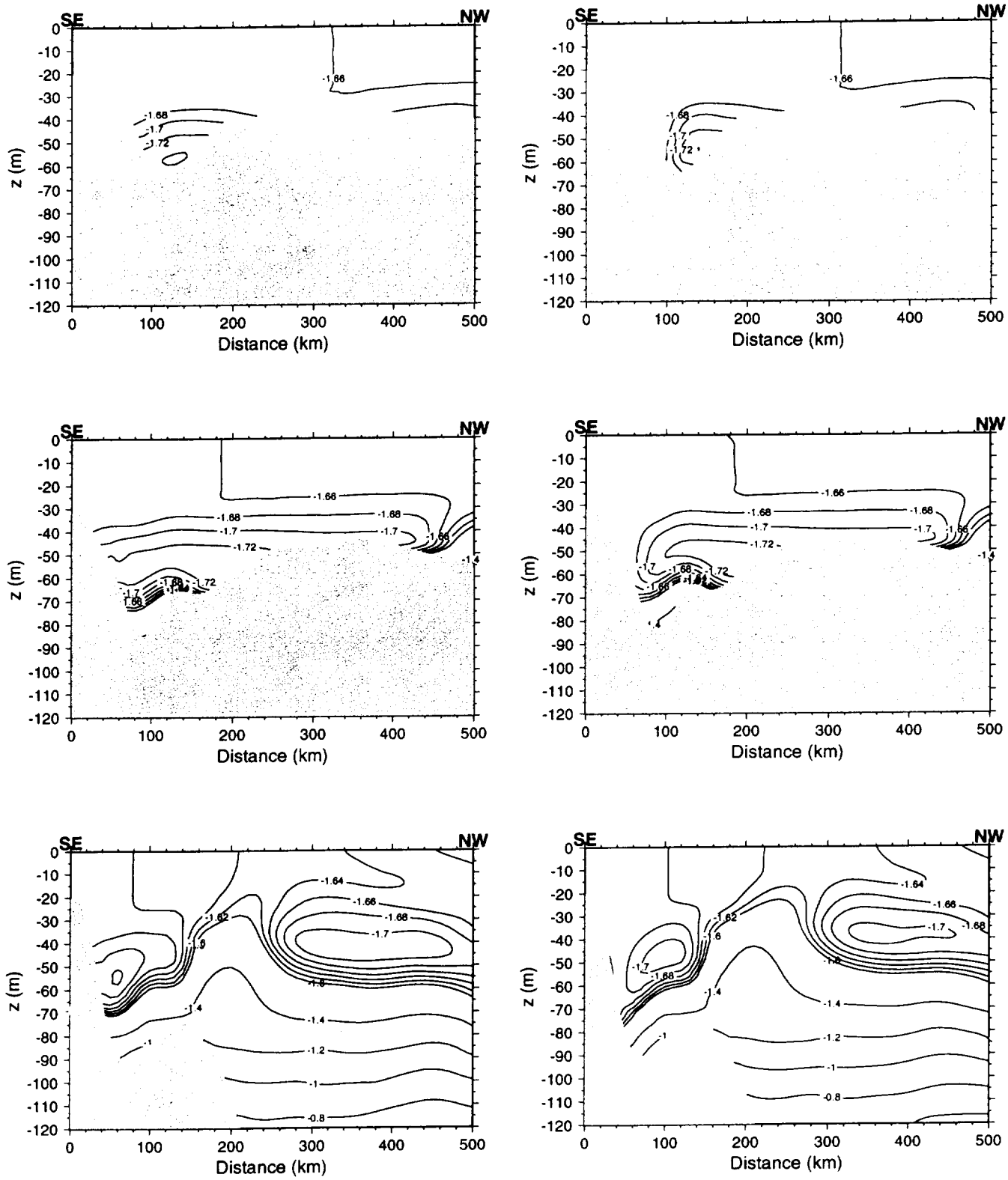

Figure 12. Temperature sections after 30 days from model runs with (case2, right) and without (case 3, left) coastal flow. Heat and salt surface fluxes from polynya are imposed on both cases. Temperatures are shown at 3 transects perpendicular to the coast and across the polynya brine generation area. Note that these transects are also perpendicular to Barrow Canyon. The contours are 0.02 for $T \leq -1.6°C$ and 0.2 for $T \geq -1.6°C$.

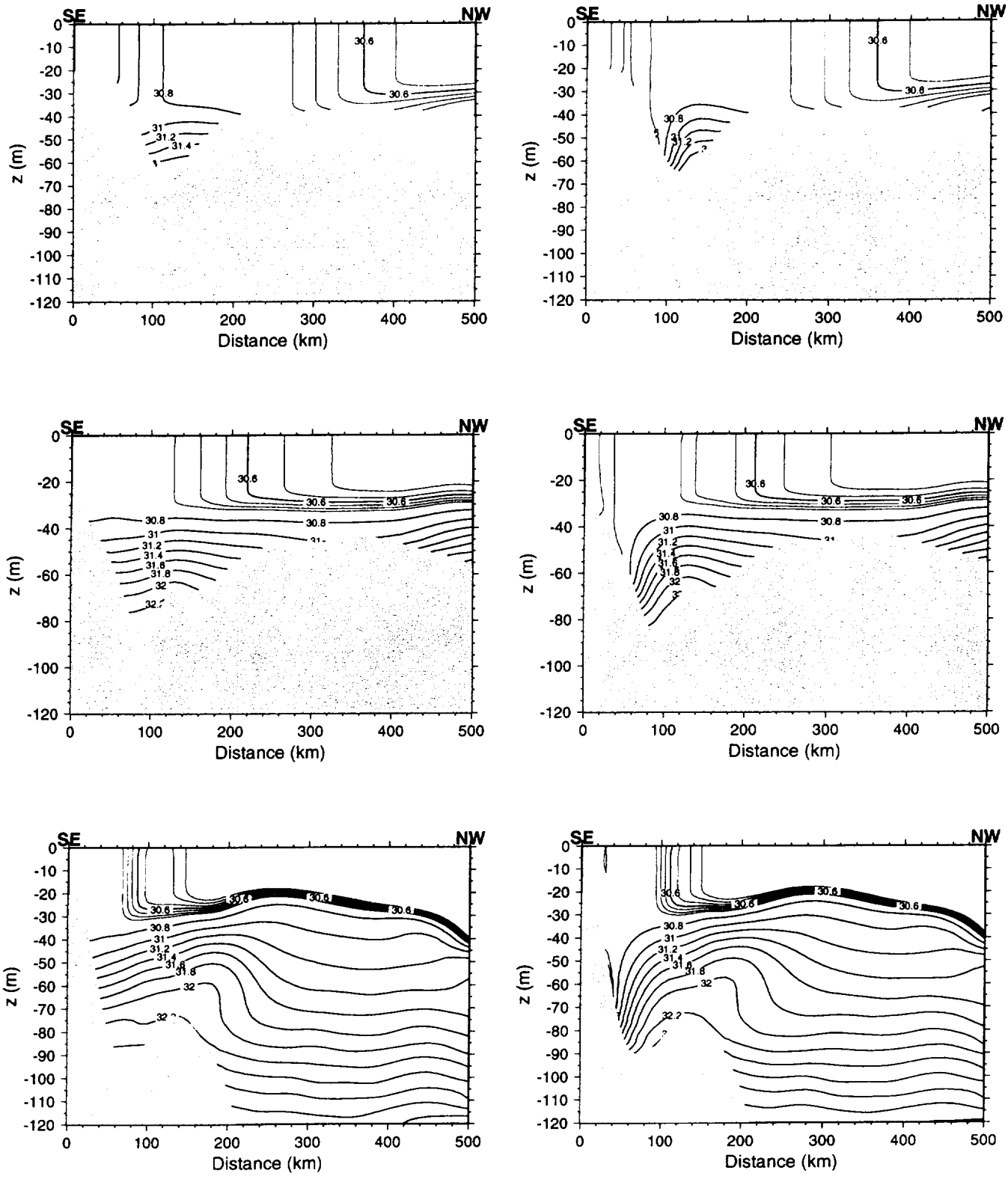

Figure 13. Salinity sections after 30 days from model runs with (case2, right) and without (case 3, left) coastal flow. Heat and salt surface fluxes from polynya are imposed on both cases. Salinities are shown at 3 transects perpendicular to the coast and across the polynya brine generation area. Note that these transects are also perpendicular to Barrow Canyon. The contours are 0.1 for $S \leq 30.7$ psu and 0.2 for $S \geq 30.7$ psu.

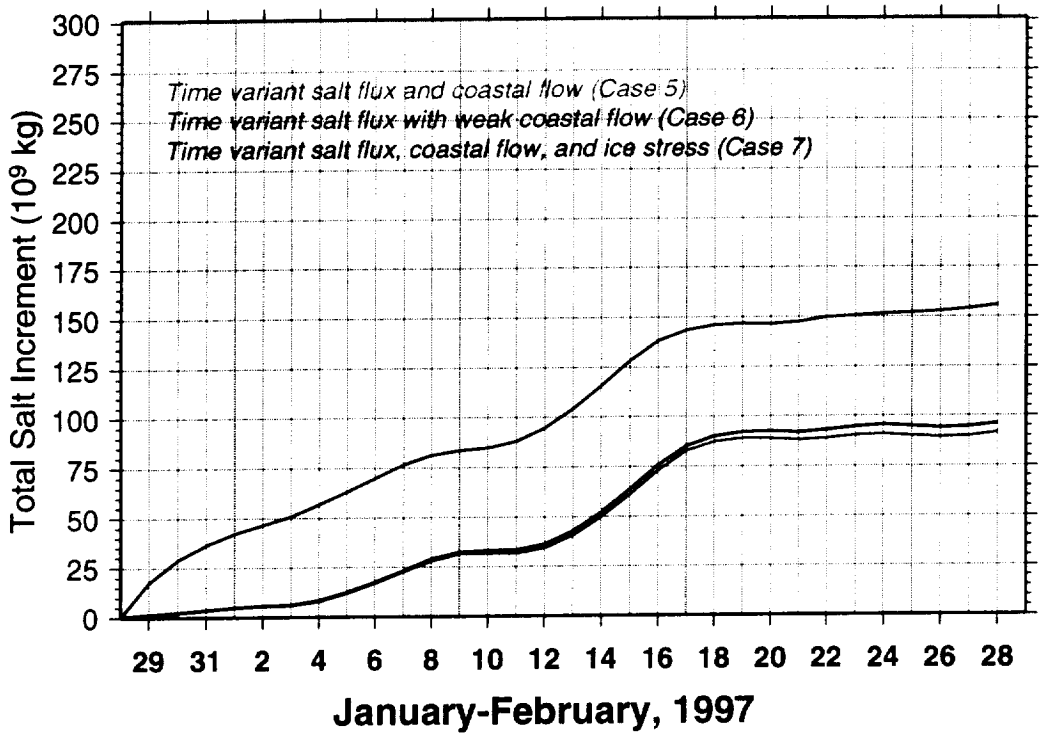

Figure 14. Total salt increment, in 10^9 kg, within the control volume shown in Figure 4 for three different numerical experiments (cases 5, 6, and 7). The simulation was conducted for the period of January 28 through February 28, 1997. The total polynya salt production for this time period was 223×10^9 kg. Case 5 was forced by time-variant surface fluxes (salt and heat) and time-variant coastal current. Case 6 was forced by time-variant surface fluxes and a very weak and steady coastal current. The forcing for case 7 was similar to case 5, except that time-variant ice-water stress was also imposed at the surface. The total salt accumulated within the control volume after 32 days of simulation for cases 5, 6, and 7 are, respectively, 92×10^9 kg, 155×10^9 kg, and 96×10^9 kg.

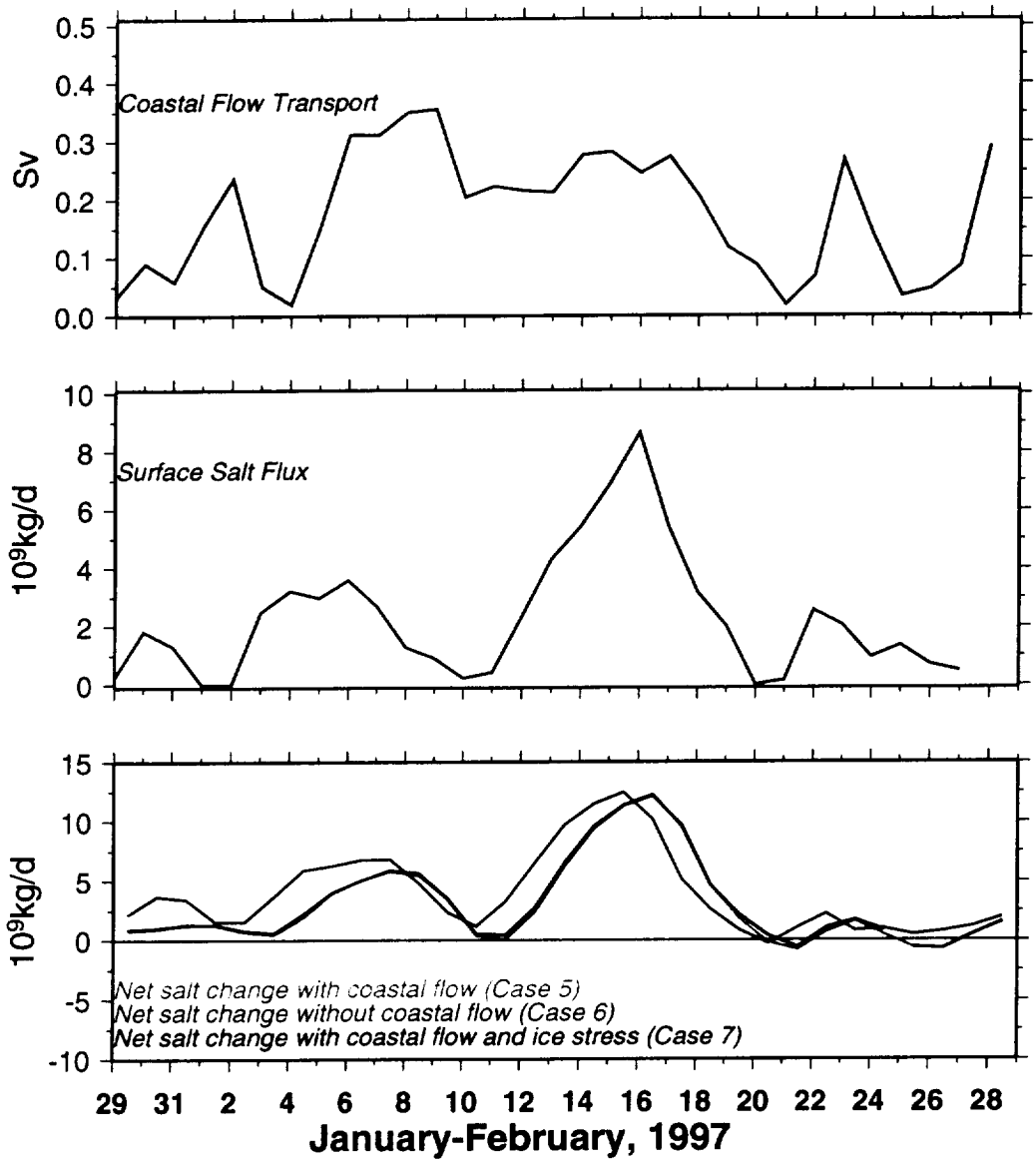

Figure 15. Time series of coastal flow transport, surface salt flux from polynyas, and net salt change due to polynya production and horizontal transport for January 28-February 28, 1997. The net salt change time series are shown for 3 simulations: (1) surface heat/salt flux forcing with coastal flow (case 5); (2) surface heat/salt flux forcing with weak and steady coastal flow (case 6); and (3) surface heat/salt flux forcing, surface ice stress forcing, and coastal flow (case 7). Daily salt/heat fluxes and coastal flow transport are used in these simulations. Daily surface ice stress is also used to force the run for case 7.

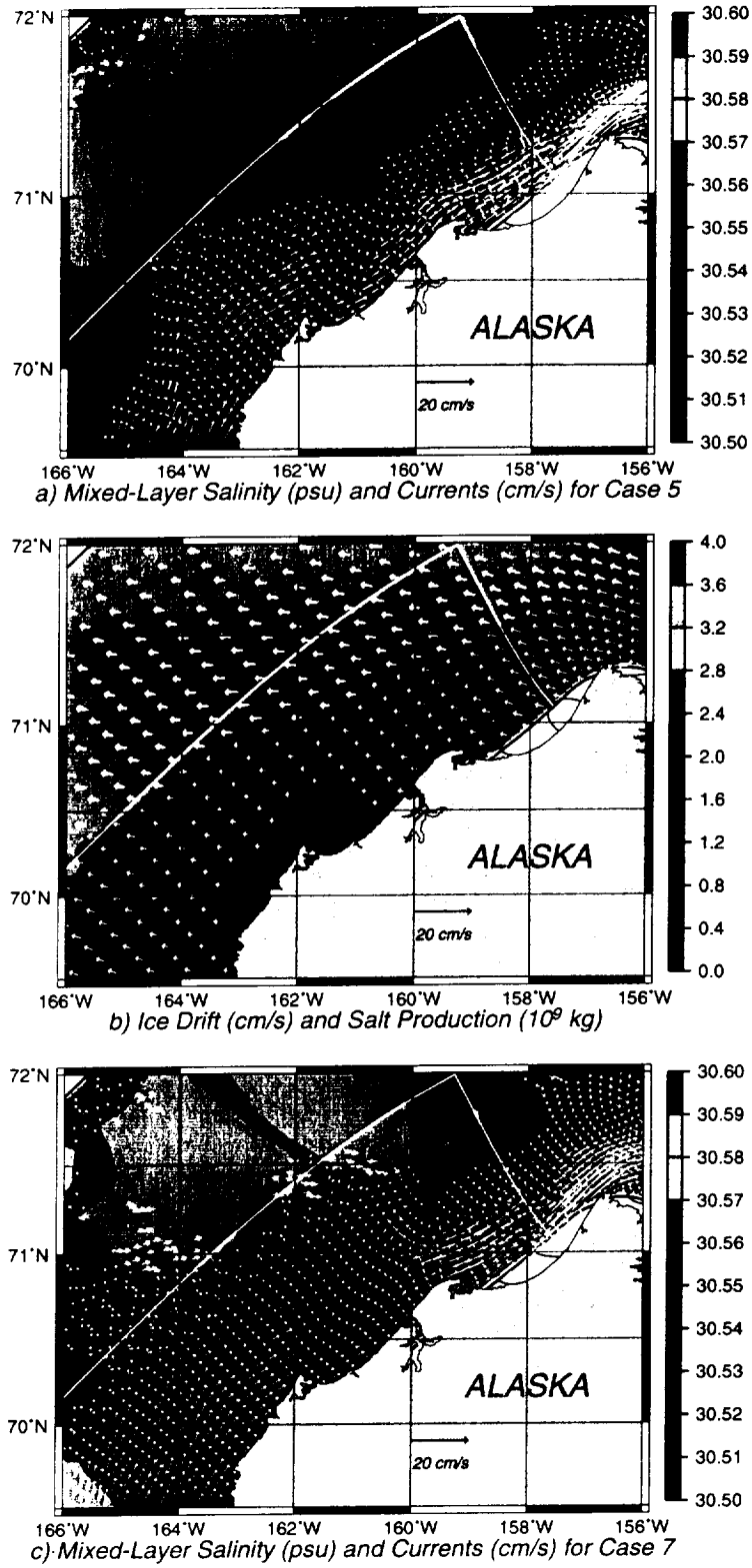

Figure 16. Salinity distribution and currents for case 5 (a) and case 7 (c) simulations, and ice drift and salt production (b) for January 28 - February 28, 1997. The white rectangle delimits the control volume for the calculation of the salt production budget. Case 5 is forced with time-variant salt/heat fluxes and coastal flow. Case 7 is forced with time variant salt/heat fluxes, coastal flow, plus ice-ocean surface stress. The ice drift is primarily against the coastal flow, thus reducing its intensity. Note that the cyclonic flow in the eastern side of the control volume shown in case 5 is dampened by the surface ice stress in case 7. Both salinity and currents were depth- (surface to 30 meters) and time-averaged (30 days). The ice drift was averaged over the 30-day period while the salt production is summed over the same time period. Current and ice drift vectors with amplitude $\leq$ 2 cm/s are not plotted.

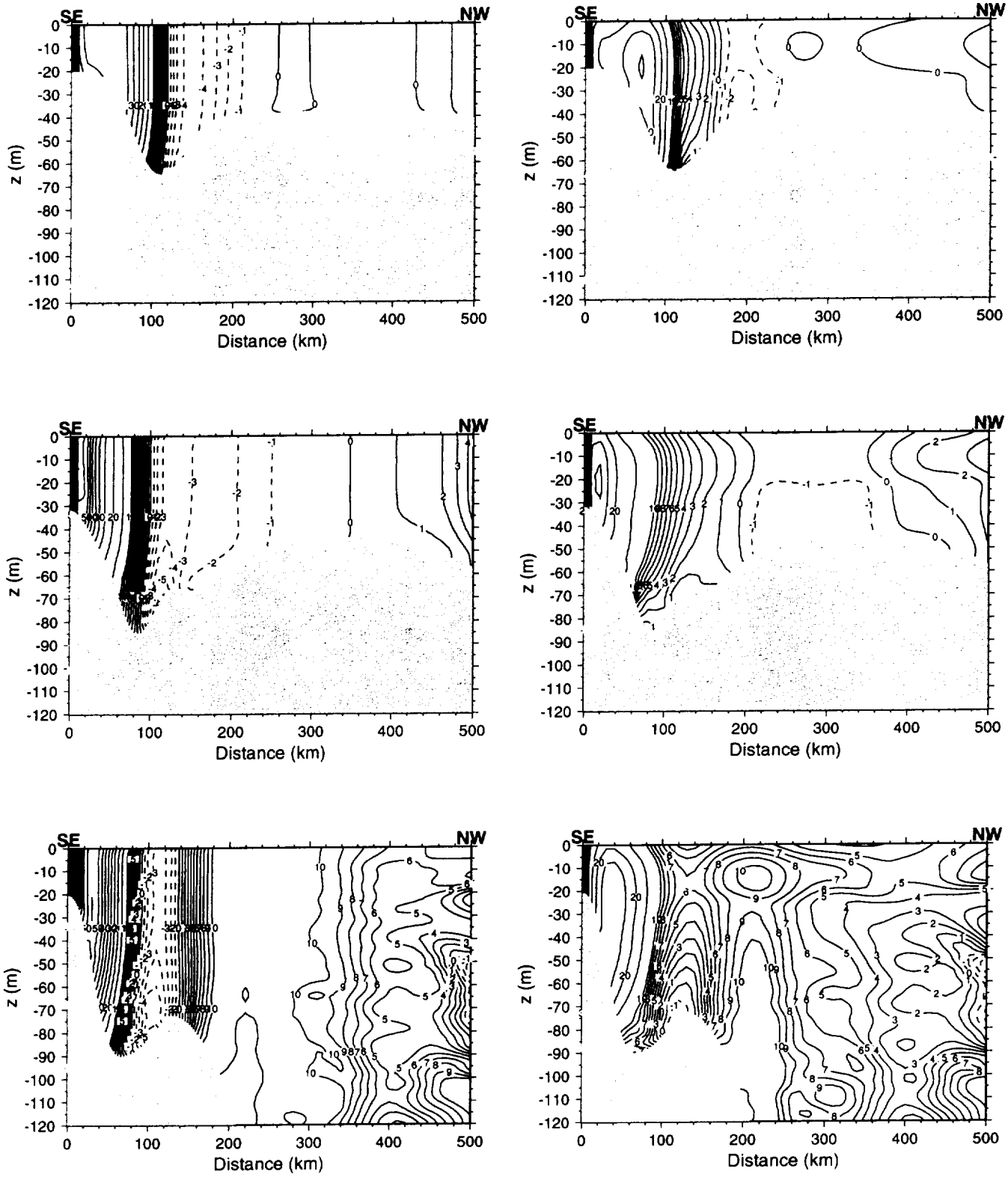

Figure 17. Thirty-day averaged sections of u-component of velocity from model runs with (case 6, right) and without (case 5, left) surface ice stress. The u-component is shown at 3 transects perpendicular to the coast and across the polynya brine generation area. Note that these transects are also perpendicular to Barrow Canyon. The contour intervals are 1 cm/s for $u \leq 10$ cm/s and 5 cm/s for $u \geq 10$ cm/s.

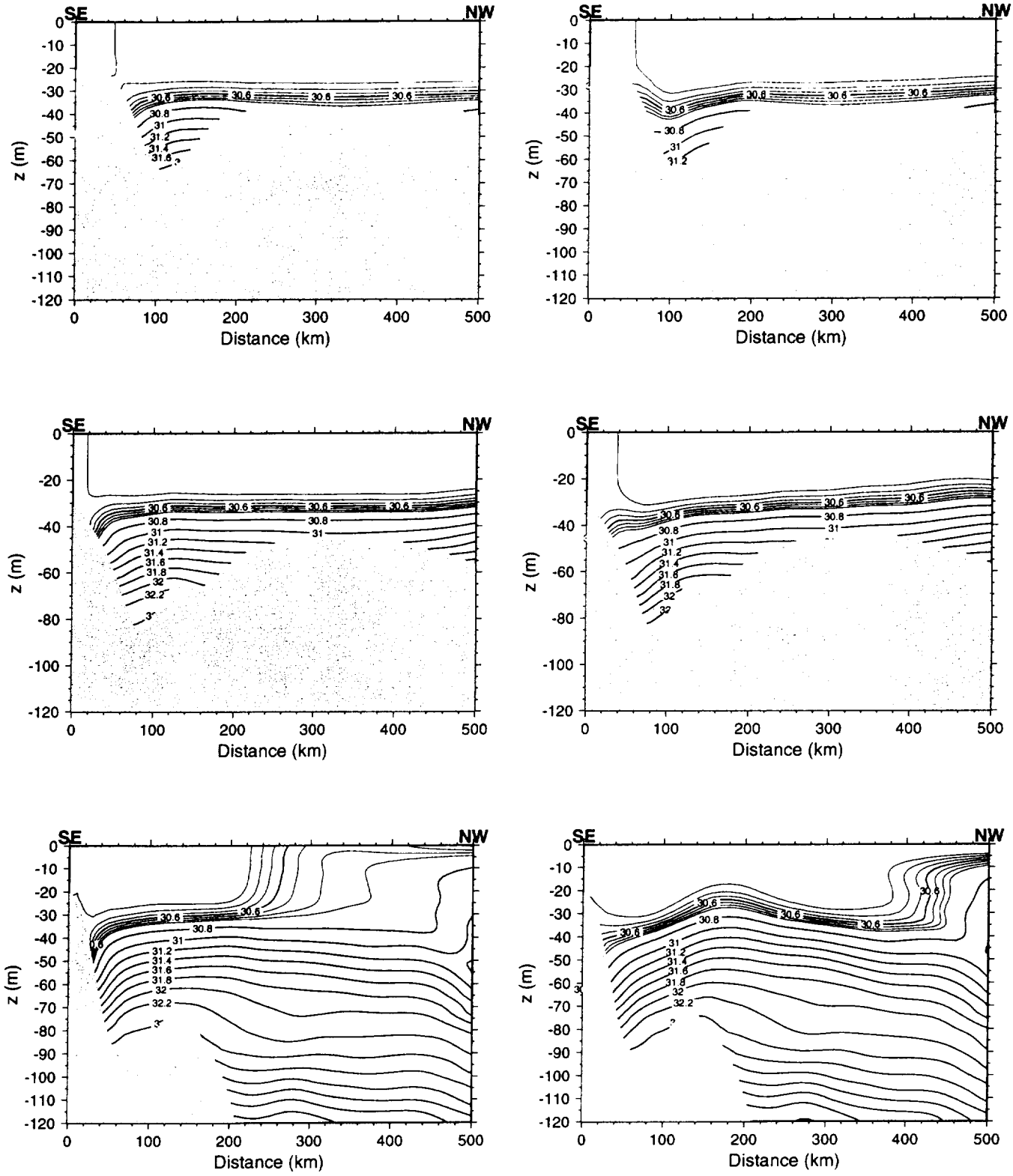

Figure 18. Thirty-day averaged sections of salinity from model runs with (case 6, right) and without (case 5, left) surface ice stress. The salinity is shown at 3 transects perpendicular to the coast and across the polynya brine generation area. Note that these transects are also perpendicular to Barrow Canyon. The contour intervals are 0.1 for $S \leq 30.7$ psu and 0.2 for $S \geq 30.7$ psu.

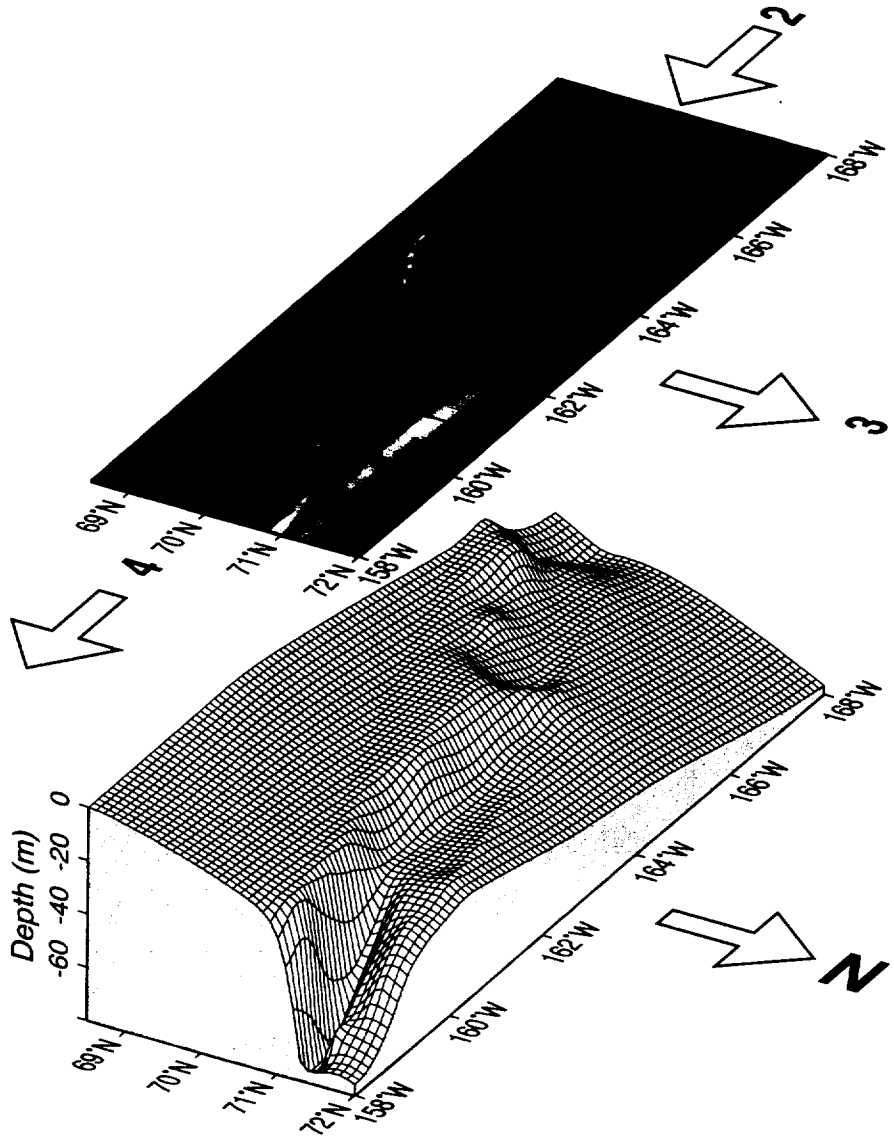

Figure 19. Mean salinity distribution and three dimensional rendition of bottom topography within the domain of the control volume box. The salt exchange pathways are shown by the large arrows. The polynya salt production enters the control volume via the surface flux (1). Most of the exported salt leaves the control volume via strong advection imparted by the swift flow at the southern flank of Barrow Canyon (4). The lateral exchange via the west (2) and northern boundaries (3) is relatively much smaller. For case 7, for which the forcing fields are the most realistic (time-variant surface salt flux, coastal current, and surface ice-water stress), the total salt accumulated for the 32-day simulation (January 28 - February 28, 1997) within the shelf region delimited by the control volume is 96×10^9 kg. The total salt production by the polynya for the same time period is 223×10^9 kg. The difference of 127×10^9 kg is primarily exported via Barrow Canyon by the coastal current.